R-matrix analysis of ^{16}O compound nucleus reactions

R. J. deBoer,[1,*] J. Görres,[1] G. Imbriani,[1,2] P. J. LeBlanc,[1] E. Uberseder,[1] and M. Wiescher[1]
[1]*Department of Physics, University of Notre Dame, Notre Dame, Indiana 46556, USA*
[2]*Università degli Studi di Napoli "Federico II" and INFN, Napoli, Italy*
(Received 2 October 2012; revised manuscript received 20 November 2012; published 16 January 2013)

Background: Over the past 60 years, a large amount of experimental nuclear data have been obtained for reactions which probe the ^{16}O compound nucleus near the α and proton separation energies, the energy regimes most important for nuclear astrophysics. Difficulties and inconsistencies in *R*-matrix fits of the individual reactions prompt a more complete analysis.
Purpose: Determine the level of consistency between the wide variety of experimental data using a multiple entrance/exit channel *R*-matrix framework. Using a consistent set of data from multiple reaction channels, attain an improved fitting for the ^{15}N$(p,\gamma_0)^{16}$O reaction data.
Methods: Reaction data for all available reaction channels were fit *simultaneously* using a multichannel *R*-matrix code.
Results: Over the wide range of experimental data considered, a high level of consistency was found, resulting in a single consistent *R*-matrix fit which described the broad level structure of ^{16}O below $E_x = 13.5$ MeV. The resulting fit was used to extract an improved determination of the low-energy *S* factor for the reactions ^{15}N$(p,\gamma)^{16}$O and ^{15}N$(p,\alpha)^{12}$C.
Conclusion: The feasibility and advantages of a complete multiple entrance/exit channel *R*-matrix description for the broad level structure of ^{16}O has been achieved. A future publication will investigate the possible effects of the multiple-channel analysis on the reaction ^{12}C$(\alpha,\gamma)^{16}$O.

DOI: 10.1103/PhysRevC.87.015802 PACS number(s): 26.20.Cd, 26.20.Fj, 21.10.Tg, 25.40.Lw

I. INTRODUCTION

The nucleus ^{16}O plays a key role for the evolution of baryonic matter in our universe. Its pronounced α-cluster structure is responsible for the closing of the CN cycle through the ^{15}N$(p,\alpha)^{12}$C reaction, controlling the stellar hydrogen burning in massive main sequence stars and determines the strength of the ^{12}C$(\alpha,\gamma)^{16}$O reaction that defines the ^{12}C/^{16}O ratio in stellar helium burning, which in turn influences the burning sequence during late stellar evolution, the ignition conditions of thermonuclear supernovae, and, last but not least, the formation of organic life on habitable planets such as Earth.

In terms of the hydrogen burning pattern, the level structure of the compound nucleus ^{16}O influences the branching of ^{15}N$(p,\gamma)^{16}$O versus ^{15}N$(p,\alpha)^{12}$C, feeding the second NO cycle [1], and characterizes the end point of stellar helium burning, ^{12}C$(\alpha,\gamma)^{16}$O, which is dubbed the "Holy Grail" of nuclear astrophysics [2,3]. To investigate the specific role of the ^{16}O nucleus for these reactions, a wealth of experimental data have been accumulated over the past few decades, including studies of ^{12}C$(\alpha,\alpha_0)^{12}$C, ^{12}C$(\alpha,\alpha_1)^{12}$C, ^{12}C$(\alpha,p)^{15}$N, ^{12}C$(\alpha,\gamma)^{16}$O, ^{15}N$(p,p)^{15}$N, ^{15}N$(p,\alpha_0)^{12}$C, ^{15}N$(p,\alpha_1)^{12}$C, ^{16}N$(\beta\alpha)^{12}$C, and ^{15}N$(p,\gamma)^{16}$O. These reactions are characterized by strong, broad, and interfering resonances as well as direct radiative capture processes, all directly associated with the single-particle and α-cluster configuration of the nucleus.

The critical excitation energy range in ^{16}O covers the broad range between and beyond the α and proton separation energies ($S_\alpha = 7.16191$ and $S_p = 12.12741$ MeV, respectively [4]). The complexity of the reaction mechanisms of $^{15}\mathrm{N} + p$ and $^{12}\mathrm{C} + \alpha$ have made it extremely difficult to determine the reaction cross sections and subsequently the reaction rates in the specific range of stellar burning with the desired accuracy and precision. Numerous attempts in the past using a variety of theoretical approaches from cluster models to multilevel *R*-matrix formalisms have provided some guidance in extrapolating the experimental data to the stellar energy range but have fallen short in rendering results with the desired precision and accuracy due to the complexity of the interplay between the different reaction channels. This paper makes a first attempt to perform a multiple-entrance-/exit-channel *R*-matrix analysis of all of the relevant experimental data, taking simultaneously into account all open reaction channels. This approach allows one to probe not only the impact of single-level resonance parameters within one or two reaction channels of a specific reaction but also the impact of the coupling of parallel competing channels on the reaction cross section in the energy range of stellar burning.

The reaction ^{15}N$(p,\gamma_0)^{16}$O is of particular importance for modeling the CNO bi-cycle as it competes with the reaction ^{15}N$(p,\alpha)^{12}$C to determine the branching between the CN and NO cycles. Several previous analyses have reported a broad range of values for the zero-energy *S* factor $S(0)$ [5–9]. The large uncertainty in $S(0)$ results from three competing contributions to the cross section. These include a resonant contribution from the two 1^- levels in ^{16}O at $E_x = 12.45$ and 13.09 MeV, external radiative capture to the ground state, and the tails of higher-energy resonances. All three contributions conspire to create a complex interference pattern that has not been satisfactorily reproduced by a physically consistent *R*-matrix fit.

*rdeboer1@nd.edu

The present analysis focuses primarily on extrapolating the low-energy S factor of the reaction ^{15}N$(p,\gamma)^{16}$O into the stellar energy range. This has been motivated by the recent work of Refs. [9] and [10] where several R-matrix fits have been made to the recent ^{15}N$(p,\gamma_0)^{16}$O data of Ref. [10]. Reference [10]'s analysis achieved good agreement between the experimental data and the R-matrix fit, but did so by allowing all the R-matrix fit parameters to vary freely even though some parameters were not well constrained by the ^{15}N$(p,\gamma)^{16}$O data alone. The fit resulted in a value for the proton asymptotic normalization coefficient (ANC) of the ground state which was considerably larger than that reported in Ref. [8] where the ANC could be measured more accurately and precisely using the ^{15}N(^{3}He, d)^{16}O transfer reaction. The recent publication of Ref. [9] demonstrated that good R-matrix fits could be obtained to the data even if the value of the ground-state proton ANC was fixed to that of the transfer reaction measurement if a background pole was also included in the R-matrix analysis. Reference [9] also emphasized that partial width measurements, using alternative particle reaction channels, should be considered in order to achieve a more physically consistent R-matrix fit. The present analysis takes both of these ideas into consideration by constraining the partial widths directly using a global multiple-entrance-/exit-channel R-matrix approach to simultaneously fit a wide range of experimental data from the literature and by fixing the proton ANC of the ground state to the value given in Ref. [8].

Section II summarizes the criterion used for data set inclusion in the global analysis. Section III details the general aspects of the R-matrix approach used in this work. Section V begins by reexamining the R-matrix analysis of only the ^{15}N$(p,\gamma_0)^{16}$O data in order to motivate the multiple-entrance-/exit-channel R-matrix analysis. The remainder of this section details the global analysis for each particle reaction channel. Discussions of the results of the analysis are presented in Sec. VI and the section concludes with the extrapolation of the ^{15}N$(p,\gamma_0)^{16}$O excitation curve with the constraints imposed by the other reaction-channel data. Finally, conclusions are presented in Sec. VII.

II. SELECTED DATA

A few key criteria are used to select the data appropriate for this analysis from the numerous reaction data available for the ^{16}O nucleus in the literature. First, the excitation energy range is limited to $E_x < 14$ MeV ($E_\alpha < 9$ MeV, $E_p < 2$ MeV), excluding several experiments which reported excitation curves at higher energies (e.g., Refs. [11–14]). It was attempted to expand the analysis to higher energies, but because of the presence of many broad overlapping and interfering resonances, some of which remain uncharacterized, reasonable fits could not be obtained. The second criterion is the availability of data. Above $E_x = 14$ MeV there is only a limited amount of measurements for several of the reaction channels. The third criterion is that the data be approximately free of target effects. That is, the total width of the resonances examined should be much greater than the energy loss of the beam through the experimental target. Some data sets have small sections of their excitation curves that are dominated by narrow resonances where this criterion is not met (e.g., Refs. [15,16]). These excitation curves are still included but the small sections of the excitation curves curves covering these resonances are removed. The contributions from these narrow resonances were tested by doing calculations where energies and partial widths from the literature [17] were used. None of the omitted levels were found to have any effect on the fitting. Table I summarizes the previous works included in this analysis.

III. *R*-MATRIX APPROACH

An R-matrix code, based on the principles developed for the code AZURE [41], is used for the present analysis. A detailed description of the original AZURE code and the underlying R-matrix theory can be found in Refs. [41,42] and references therein. The present code has taken the computational concepts and physics of the original code and reimplemented them in an object oriented approach using C++. A result of the new coding structure is that multiple-entrance-/exit-channel analysis is naturally implemented. To decrease computation times, the code supports multiprocessor computations using OPENMP[1] and by way of MINUIT2 [43], which is used for the fit minimization.

This R-matrix analysis of the ^{16}O compound nucleus considers two particle entrance channels, $^{12}\mathrm{C}+\alpha_0$ and $^{15}\mathrm{N}+p$, and four particle exit channels, $^{12}\mathrm{C}+\alpha_0$, $^{12}\mathrm{C}\alpha_1$, $^{16}\mathrm{O}\gamma$, and $^{15}\mathrm{N}+p$ (see Fig. 1). The $^{16}\mathrm{O}+\gamma$ exit channel is further subdivided into the different γ-ray deexcitation channels. The resonances parameters of the channels that are considered are summarized in Tables VIII, IX, and X of Appendix A. Initial values for resonance energies, widths, and spin parties are taken from Ref. [17] or from the data publications listed in Table I. These values are often found to be reasonably consistent and usually provide a good starting point for the R-matrix fit. The R-matrix radii and particle separation energies, in use throughout the analysis, are given in Table II. Cross sections, S factors, and partial widths throughout this work are *always in the center-of-mass system*. In figures, energy scales are given in terms of the excitation energy of the ^{16}O compound nucleus for more convenient comparison of the different reaction channel data as well as laboratory energy (i.e., proton energy or E_α) for more convenient viewing by experimentalists. The external capture model (e.g., Refs. [41,44,45]) is used for nonresonant γ-ray cross-section contributions. Fits are performed using the alternative R-matrix parametrization described in Ref. [46] which allows for observable parameters to be fit directly and eliminates the need for a boundary conditions or level shifts. As a consistency check, calculations have been checked against those performed with the code of Ref. [47].

IV. INITIAL ^{15}N$(p,\gamma_0)^{16}$O ANALYSIS

In the previous work of Ref. [10], only the ^{15}N$(p,\gamma_0)^{16}$O data were used for an R-matrix analysis, with the partial widths

[1]The OPENMP name and the OPENMP logo are registered trademarks of the OPENMP Architecture Review Board.

TABLE I. Summary of references and associated reactions considered in this work for the *R*-matrix analysis of ^{16}O. Targets are also given, where the percentage always indicates the enrichment in either ^{15}N or ^{12}C.

Ref.	Reaction(s)	Targets
Schardt *et al.* [18] (1952)	^{15}N$(p,\alpha_0)^{12}$C	KNO_3 (61%),TiN
Hagedorn [19] (1957)	^{15}N$(p,p)^{15}$N	^{15}N implanted in C,KNO_3 (61%)
Hagedorn and Marion [20] (1957)	^{15}N$(p,\alpha_0)^{12}$C	^{15}N implanted in Be
Bashkin *et al.* [21] (1959)	^{15}N$(p,p)^{15}$N, ^{15}N$(p,\alpha_0)^{12}$C, ^{15}N$(p,\alpha_1)^{12}$C	^{15}N gas (95 or 98%)
Hebbard [5] (1960)	^{15}N$(p,\gamma_0)^{16}$O	TiN
Larson and Spear [22] (1964)	^{12}C$(\alpha,\gamma_0)^{16}$O	Enriched ^{12}C acetylene on Ta
Mitchell and Ophel [23] (1965)	^{12}C$(\alpha,\alpha_1)^{12}$C, ^{12}C$(\alpha,p)^{15}$N	^{nat}C foil
Morris *et al.* [24] (1968)	^{12}C$(\alpha,\alpha_0)^{12}$C	^{nat}C foil
Kernel *et al.* [25] (1971)	^{12}C$(\alpha,\gamma_0)^{16}$O	C foil (98.98%)
Brochard *et al.* [26] (1973)	^{12}C$(\alpha,\gamma_0)^{16}$O, ^{15}N$(p,\alpha_0)^{12}$C, ^{15}N$(p,\gamma_0)^{16}$O	
Rolfs and Rodney [6] (1974)	^{15}N$(p,\gamma_0)^{16}$O	TiN (99%)
D'Agostino Bruno *et al.* [27] (1975)	^{12}C$(\alpha,\alpha_0)^{12}$C	^{nat}C foil
Ophel *et al.* [28] (1976)	^{12}C$(\alpha,\gamma_0)^{16}$O	Enriched ^{12}C foil
Bray *et al.* [29] (1977)	^{15}N$(p,\alpha_0)^{12}$C	Melamine (98%)
Zyskind and Parker [30] (1979)	^{15}N$(p,\alpha_0)^{12}$C	TiN (99.9%)
Redder *et al.* [31] (1982)	^{15}N$(p,\alpha_0)^{12}$C	TiN (99%), N_2 gas jet target
Sawicki *et al.* [32] (1986)	^{15}N$(p,\alpha_0)^{12}$C	^{15}N implanted in stainless steel
Feng *et al.* [33] (1994)	^{12}C$(\alpha,\alpha_0)^{12}$C	^{nat}C foil
Schürmann *et al.* [16] (2005)	^{12}C$(\alpha,\gamma)^{16}$O	Windowless ^{4}He gas target (inv. kin.)
La Cognata *et al.* [34] (2007)	^{15}N$(p,\alpha_0)^{12}$C	Self-supporting CD_2 (trojan horse)
Tischhauser *et al.* [15] (2009)	^{12}C$(\alpha,\alpha_0)^{12}$C	^{nat}C foil
Bemmerer *et al.* [35] (2009)	^{15}N$(p,\gamma)^{16}$O	Windowless gas target of ^{nat}N
LeBlanc *et al.* [10] (2010)	^{15}N$(p,\gamma_0)^{16}$O	TiN (>98%, 82.6%)
Caciolli *et al.* [36] (2011)	^{15}N$(p,\gamma)^{16}$O	TiN (96–98%)
Schürmann *et al.* [37] (2011)	^{12}C$(\alpha,\gamma_{(0,6.05,6.13,6.92,7.12)})^{16}$O	Windowless ^{4}He gas target (inv. kin.)
deBoer *et al.* [38] (2012)	^{15}N$(p,p)^{15}$N, ^{15}N$(p,\alpha_0)^{12}$C	Windowless gas target of ^{15}N (99%)
deBoer *et al.* [39] (2012)	^{12}C$(\alpha,\alpha_0)^{12}$C, ^{12}C$(\alpha,\alpha_1)^{12}$C, ^{12}C$(\alpha,p)^{15}$N	^{nat}C foil
Imbriani *et al.* [40] (2012)	^{15}N$(p,\alpha_1\gamma)^{12}$C, ^{15}N$(p,\gamma_{(6.05,6.13,7.12)})^{16}$O	TiN (>98%, 82.6%)

(Γ_p, Γ_{α_0}, and Γ_{γ_0}) of the two 1^- resonances at $E_x = 12.45$ and 13.09 MeV and the strength of the proton direct capture to the ground state (ANC) allowed to vary as free fit parameters. This analysis resulted in unphysical values for some of the partial widths and for the ANC as noted in that work (Sec. IV and Fig. 9 of Ref. [10]) and Ref. [9].

Some data from Ref. [10] had been previously omitted as they required corrections for target degradation. These corrections have been made and the new data points are included in the present analysis with the correct normalization. The revised data can be found in Table XII in Appendix C.

TABLE II. Radii and particle separation energies used in the *R*-matrix calculation. Here a_α, a_{α_1}, and a_p are the ground state α, first excited state α, and ground-state proton *R*-matrix radii, respectively. The quantities S_α, S_p, and S_{α_1} represent the separation energies of an α, a proton, and a first excited state α particle from ^{16}O, respectively.

Parameter	Value	Ref.
a_α,a_{α_1}	5.43 fm	[48]
a_p	5.03 fm	[49]
S_α	7.16192(1) MeV	[4]
S_p	12.12741(1) MeV	[4]
S_{α_1}	11.60083(31) MeV	[4]

Recently it was suggested [9] that the proton ANC of the ground state be treated as a fixed parameter in the *R*-matrix analysis since the value of 13.9(19) fm$^{-1/2}$, as determined in an independent transfer reaction experiment [8], is much better constrained than the value that would be extracted from the ^{15}N$(p,\gamma_0)^{16}$O cross-section data. This suggestion was followed in the present analysis.

Before discussion of the multiple-particle-channel analysis, the single-particle-channel analysis is briefly revisited. As a first step, a fit similar to that of Ref. [10] is reproduced. In addition, several other fitting techniques are tested using different permutations of ANC values and background pole assumptions as given in Table III. While low values of χ^2 are achieved in several of the fits, the lack of constraint on the partial widths and ANC inhibit the identification of unique fit parameters for the various reaction contributions.

Fit 1 in Table III allows the ANC to float as a free parameter and results in a value for the ANC of 23 fm$^{-1/2}$, as was found in Ref. [10], compared to the value of 13.9(19) fm$^{-1/2}$ found in the transfer experiment of Ref. [8]. This demonstrates that the ^{15}N$(p,\gamma_0)^{16}$O data alone cannot sufficiently constrain the value of the ANC and all the allowed decay widths as noted in Ref. [10].

A second fit is performed where the value of the ANC is fixed to that given in Ref. [8], yet a reproduction of the data of similar quality cannot be obtained as demonstrated by

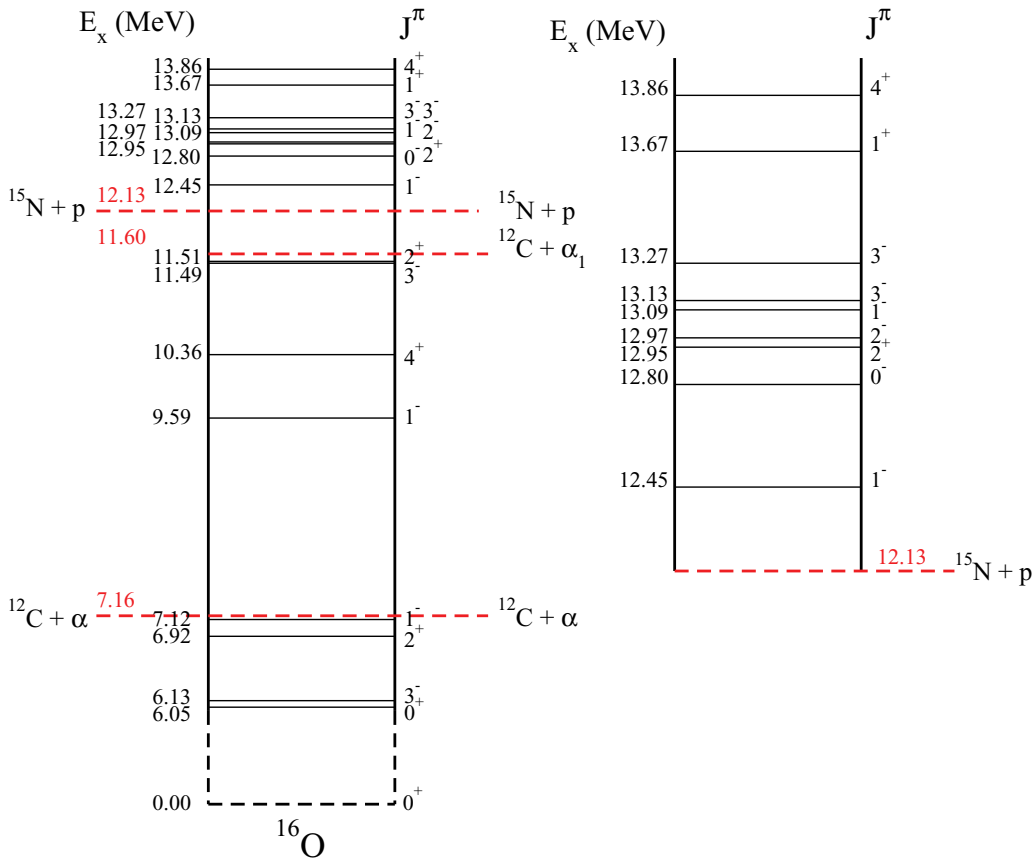

FIG. 1. (Color online) The diagram on the left shows the level structure of ^{16}O up to $E_x = 14$ MeV. Only levels and subthreshold states included in this analysis are shown (see Table VIII of Appendix A). On the right is an enlarged view of the energy region above the proton separation energy at $E_x = 12.13$ MeV. Entrance (exit) channels are displayed on the left (right). Particle separation energies are indicated by horizontal red dashed lines. Excitation energies are in units of MeV.

the large reduced χ^2 of Fit 2. This implies that the external capture cannot fully describe the direct component of the cross section over the energy range of the experimental data and that a background pole component is necessary to provide a significant internal contribution.

Fit 3 uses a fixed value for the ANC and includes a background pole whose energy is fixed. The fit is found to be insensitive to the exact energy of the background pole, when the partial widths are allowed to vary freely, and a value of $E_x = 20$ MeV is chosen purely for convenience. The proton and γ_0 partial widths are allowed to vary freely. With the inclusion of the background pole, a fit of similar quality as Fit 1 can be achieved. It is important to note that the proton and γ_0 widths of the background pole are highly correlated with each other. That is, similar fits could be achieved if the ratio of the widths are roughly constant.

TABLE III. Summary of the different preliminary techniques used to fit the ^{15}N$(p,\gamma_0)^{16}$O data of Ref. [10]. Here BGP refers to the background pole, ANC to the asymptotic normalization coefficient, and $S(0)$ to the value of the astrophysical S factor at nearly zero energy ($E_{\text{c.m.}} = 10$ keV).

Index	Γ_p^{BGP} (MeV)/$\Gamma_{\gamma_0}^{\text{BGP}}$ (eV)	ANC$_{\text{gs}}$ (fm$^{-1/2}$)	χ^2/N	$S(0)$ (keV b)
1	(None)	21.6 (Free)	1.7	38.8
2	(None)	13.9 (Fixed) [8]	2.5	34.9
3	6.6/170 (Free)	13.9 (Fixed) [8]	1.7	38.3
4	$0.43/6.0 \times 10^4$ (Free)	(None)	1.7	37.2
5	9.0/63 (Free)	19.4 (Free)	1.7	38.4
6	(None)	(None)	7.2	27.9

Fits 4 through 6 in Table III show alternative parameter permutations that all lead to reasonably good-quality fits, except for Fit 6, which excluded the direct capture and the background pole contributions. An extrapolation of the different fits provides an estimate of the range of uncertainty for the low-energy S factor $S(0)$. It is interesting to note that, as observed in Ref. [10], the extrapolation of the S factor to low energy is very similar for fits with similar χ^2 values, even when the fit parameters differ.

Results of the different fits are listed in Table III. Fits 1, 3, 4, and 5 all produce very similar χ^2 values. Only fits which do not include a background pole component (Fits 2 and 6) deviate substantially. Figure 2 shows Fits 2, 3, and 6. Fit 3 is representative of Fits 1, 4, and 5, which are not shown in the figure but have similar energy dependence and comparable χ^2 values.

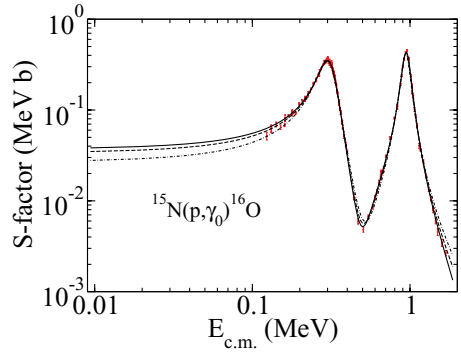

FIG. 2. (Color online) The ^{15}N$(p, \gamma_0)^{16}$O data from Ref. [10]. The dotted-dashed, solid, and dashed lines correspond to Fits 6, 3, and 2 from Table III, respectively.

Another set of important parameters for a more physical fit are the partial widths of the two resonances. Their impact is particularly visible in a variety of reactions populating the compound resonances through different particle channels. The two ^{16}O compound resonances that dominate the ^{15}N$(p, \gamma_0)^{16}$O reaction are the two 1^- excited states at $E_x = 12.45$ and 13.09 MeV excitation energy. These states can decay through the ground-state proton channel (Γ_p), the ground-state α channel (Γ_{α_0}), the first excited state α_1 channel (Γ_{α_1}), and several γ channels (associated partial widths are given in parentheses). For both resonances the ground-state γ channel (Γ_{γ_0}) dominates Γ_γ. Decays through the α_1 channel are ignored at this stage. It is later demonstrated that, for both resonances, these widths are small compared to the total width and have a limited effect on the low-energy S factor (Sec. VI C).

The single level Breit-Wigner resonance formalism is a useful tool for illustrating the limitations if considering only the ^{15}N$(p, \gamma_0)^{16}$O data for constraining the partial widths,

$$\sigma(E) \approx \pi \lambda\!\!\!^{-2} \omega \frac{\Gamma_p \Gamma_{\gamma_0}}{(E - E_R)^2 + (\Gamma/2)^2}, \qquad (1)$$

where E_R is the resonance energy, ω is the statistical factor, Γ is the total width, and $\lambda\!\!\!^{-}$ is the de Broglie wavelength divided by 2π. For the first level at $E_x = 12.45$ MeV, Γ is dominated by Γ_{α_0}, which determines the width of the resonance while the product of Γ_p and Γ_{γ_0} determines its height. For this reason the ^{15}N$(p, \gamma_0)^{16}$O data provide a reasonable constraint on Γ_{α_0} but only the product of Γ_{γ_0} and Γ_p is constrained. For the second level at $E_x = 13.09$ MeV, Γ_p is dominant. Since Γ_p now primarily determines the resonance width, it is better constrained by the data. This also provides better limits on Γ_{γ_0}. The α-partial width Γ_{α_0} is now the least constrained parameter. An example fit allowing Γ_p, Γ_{γ_0}, and Γ_{α_0} to vary as free fit parameters will then likely result in some nonunique and possibly unphysical widths like those in Table II of Ref. [10]. Clearly, additional information is necessary to achieve a physically reasonable fit as has been discussed in Ref. [10].

In order to add further constraints to the partial widths of the ^{15}N$(p, \gamma_0)^{16}$O R-matrix analysis, alternative reaction channels feeding the compound nucleus are simultaneously analyzed. This analysis includes data sets for the additional particle reaction pathways ^{12}C$(\alpha, \alpha_0)^{12}$C, ^{12}C$(\alpha, \alpha_1)^{12}$C, ^{12}C$(\alpha, p)^{15}$N,

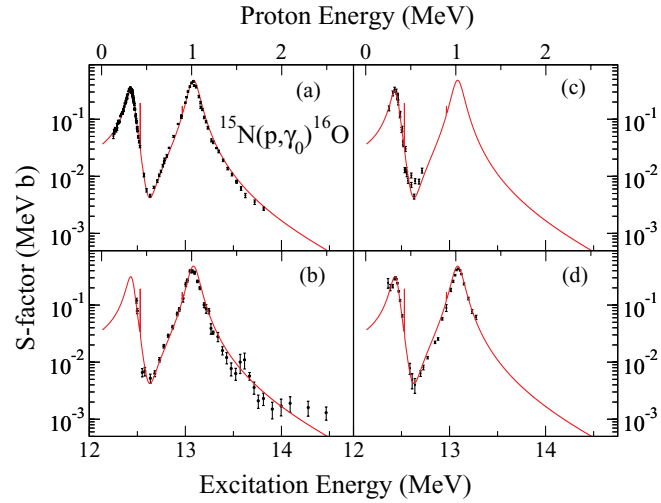

FIG. 3. (Color online) Fit to the angle-integrated ^{15}N$(p, \gamma_0)^{16}$O cross-section data of Refs. [5,6,10], and [26] labeled (a) through (d), respectively. Laboratory proton energy is given on the top horizontal axis and the excitation energy on the bottom horizontal axis of each plot.

^{12}C$(\alpha,\gamma)^{16}$O, ^{12}C$(\alpha, \gamma_0)^{16}$O, ^{15}N$(p, p)^{15}$N, ^{15}N$(p, \alpha_0)^{12}$C, ^{15}N$(p, \alpha_1)^{12}$C, ^{15}N$(p, \gamma_{(6.050)})^{16}$O, ^{15}N$(p, \gamma_{(6.130)})^{16}$O, and ^{15}N$(p, \gamma_{(7.117)})^{16}$O. The following section describes the addition of the different particle reaction pathways listed above. In each subsection, details are given about the data and which resonance transitions are used to reproduce the data.

V. MULTIPLE-CHANNEL ANALYSIS

The following subsections detail the different particle reaction channels included in this analysis. Although they are described individually, the fits to the different particle-reaction-channel data sets have been performed *simultaneously*.

A. ^{15}N$(p,\gamma)^{16}$O

Included in the analysis are the ground-state transition data from Refs. [10] (original data available at Notre Dame), [5] (digitized from Fig. 4), [6] (digitized from Fig. 2), and [26] (digitized from Fig. 3) (shown in Fig. 3), the total cross-section data from Refs. [36] (Table I) and [35] (Table III) (shown in Fig. 4), and the cascade transition data from Ref. [40] (original data available at Notre Dame) (Fig. 5). The cross-section data of Ref. [6] are truncated below $E_p = 0.37$ MeV, where the energy dependence clearly deviates from the other measurements.

B. ^{15}N$(p, \alpha_0)^{12}$C

Because of the important role of the ^{15}N$(p, \alpha_0)^{12}$C reaction for the closure of the first CNO or CN cycle and the branching to the second CNO or NO cycle, several measurements of the low-energy reaction cross section have been performed over the past few decades. Included in this analysis are the angle-integrated cross sections from Table I of Ref. [31] and those digitized from Fig. 3 of Ref. [26] (data originally from Ref. [5]) and from Table III of Ref. [34]. The Trojan horse

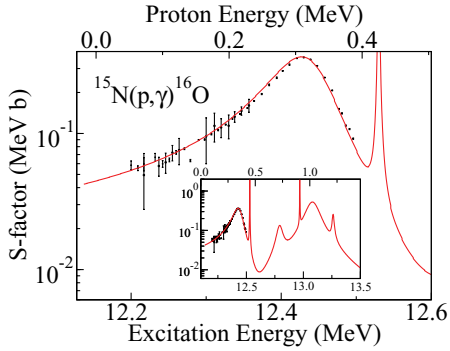

FIG. 4. (Color online) Fit to the total ^{15}N$(p,\gamma)^{16}$O cross-section data of Refs. [35,36] normalized to the R-matrix fit. The inset shows the calculation at higher energies based on the sum of the contributions from the cascade transitions of Ref. [40]. Laboratory proton energy is given on the top horizontal axis and the excitation energy on the bottom horizontal axis of the plot.

data from Ref. [34] are truncated above $E_p = 0.32$ MeV where they begin to suffer from resolution effects [50]. The data from Refs. [26,31,34] resolve the 1^- resonance at $E_x = 12.45$ MeV while the data from Ref. [26] also resolves the 1^- resonance at $E_x = 13.09$ MeV, adding constraints on the two prominent states observed in the ^{15}N$(p,\gamma_0)^{16}$O data.

Additionally, differential cross-section excitation curves are included from Refs. [21] (digitized from Figs. 4, 5, 8, and 11), [30] (Table I), [18] (digitized from Fig. 6), [20] (data for Figs. 2 and 4 obtained from EXFOR [51]), and [32] (data from Fig. 2 obtained from EXFOR [51]). The data from Refs. [18,20,32] display a 3^- state at $E_x = 13.27$ MeV. Smaller contributions to the cross section from unresolved resonances at $E_x = 12.95$ MeV (2^+) and $E_x = 13.13$ MeV (3^-) are important for reproducing the angular distributions.

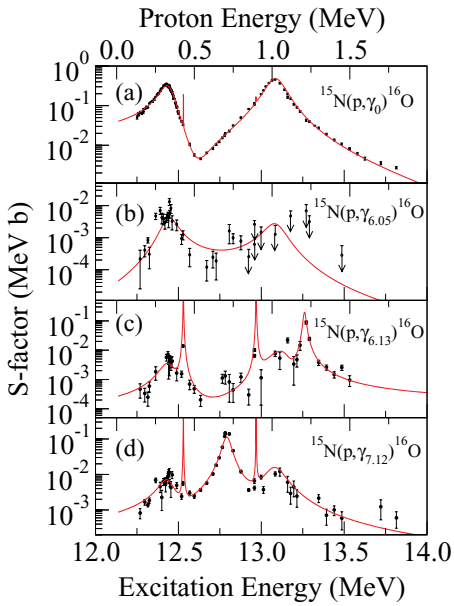

FIG. 5. (Color online) Fits to the ^{15}N$(p,\gamma_0)^{16}$O, ^{15}N$(p,\gamma_{(6.050)})^{16}$O, ^{15}N$(p,\gamma_{(6.130)})^{16}$O, and ^{15}N$(p,\gamma_{(7.117)})^{16}$O data, labeled (a) through (d), respectively, reported in Ref. [40]. Laboratory proton energy is given on the top horizontal axis and the excitation energy on the bottom horizontal axis of each plot.

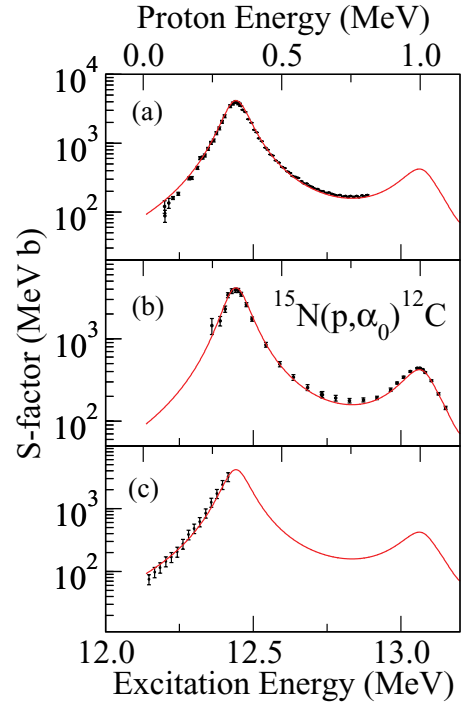

FIG. 6. (Color online) Fits to the angle-integrated ^{15}N$(p,\alpha_0)^{12}$C data of Refs. [26,31], and [34] [labeled (a) through (c), respectively]. Laboratory proton energy is given on the top horizontal axis and excitation energy on the bottom horizontal axis of each plot.

The simultaneous fit reveals differences in the energy calibration of some of the higher-energy ^{15}N$(p,\alpha_0)^{12}$C data sets of Refs. [18,20,32]. All three of these data sets had to be digitized from figures so some error in energy may be attributed to this process. In addition, in Ref. [29], note that they had to make adjustments of about 5 keV to the data of Ref. [20] in order to produce agreement with their measurements. Similar corrections are applied here. In Fig. 2 of Ref. [32] an energy offset is shown comparing their measurement to that of Refs. [18,20]. An adjustment of 5 keV upward in energy has been made to achieve better agreement for this data set.

Angular distribution data are taken from Ref. [21] (data at $E_p = 1.214$ was digitized from Fig. 6), Ref. [29] (digitized from Fig. 4), and Ref. [31] (digitized from Fig. 5). Fits to each of the data sets can be found in Figs. 6, 7, 8, 9, 10, and 11.

An additional set of ^{15}N$(p,\alpha_0)^{12}$C data was measured recently in an experiment at the Notre Dame Nuclear Science Laboratory covering the energy range $E_p = 0.6$ to 1.4 MeV. The experimental details have been published in Ref. [38]. The excitation curves were measured at $\theta_{\rm lab} = 90^\circ$, 105°, 135°, 150°, and 165°. Figure 12 shows the R-matrix fit to yield data measured at the different angles normalized to the yield data at 90°.

C. ^{15}N$(p,p)^{15}$N

Proton elastic-scattering data, just above S_p, are used from Ref. [19] (data from Fig. 3 obtained from EXFOR [51])

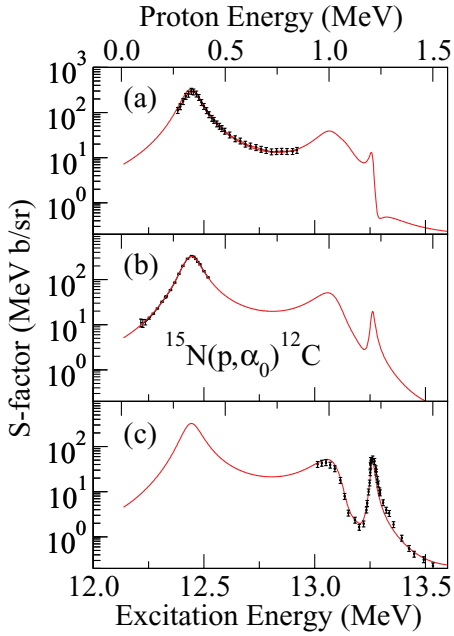

FIG. 7. (Color online) Fits to the ^{15}N(p, α_0)^{12}C differential cross-section data of Refs. [18] ($\theta_{\rm lab} = 90°$), [30] ($\theta_{\rm lab} = 135°$), and [21] ($\theta_{\rm lab} = 159.5°$) [labeled (a), (b), and (c), respectively]. Laboratory proton energy is given on the top horizontal axis and excitation energy on the bottom horizontal axis of each plot.

and Ref. [21] (digitized from Figs. 4 and 5). The data contain several unnatural parity states, including a 0^- at $E_x =$ 12.80 MeV, a 2^- at 12.97 MeV, and a 1^+ at 13.67 MeV in addition to the higher-energy 1^- state observed in the ^{15}N(p, γ_0)^{16}O data and the 3^- state at $E_x = 13.27$ MeV. Another 3^- state is also observed in this energy region at $E_x = 13.13$ MeV but does not have a significant effect in this reaction channel. The angular distributions at $E_p = 1.214$

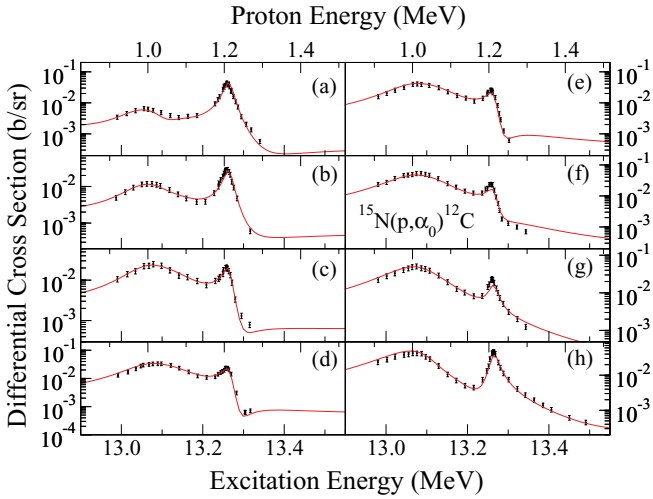

FIG. 8. (Color online) Fits to the ^{15}N(p, α_0)^{12}C differential cross sections of Ref. [20] at $\theta_{\rm lab} = 25°$, 40°, 60°, 75°, 90°, 105°, 120°, and 140° [labeled (a) through (h), respectively]. Laboratory proton energy is given on the top horizontal axis and excitation energy on the bottom horizontal axis of each plot.

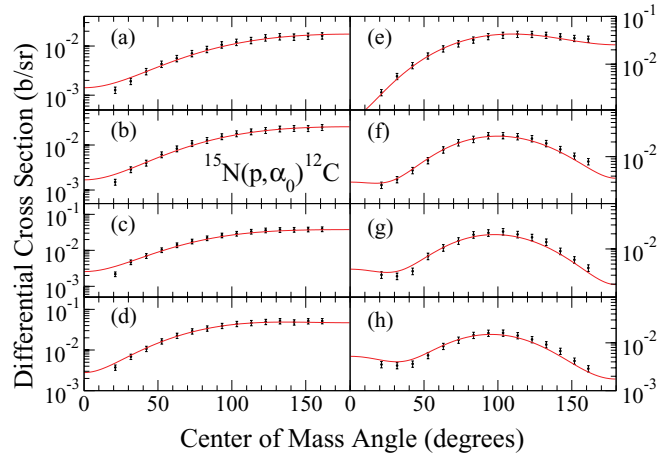

FIG. 9. (Color online) Fits to the ^{15}N(p, α_0)^{12}C angular distributions of Ref. [29] at $E_p = 0.838$, 0.888, 0.938, 0.988, 1.038, 1.088, 1.1113, and 1.138 MeV [labeled (a) through (h), respectively].

and 1.643 MeV from Ref. [21] (digitized from Fig. 7) and at $E_p = 0.65$ to 1.5 MeV from Ref. [19] (digitized from Figs. 4, 6, and 9) are also included. Fits are shown in Figs. 13, 14, 15, 16, and 17.

An additional set of ^{15}N(p, p)^{15}N elastic-scattering data were obtained in a recent experiment at the University of Notre Dame's Nuclear Science Laboratory over the energy range from $E_p = 0.6$ to 1.8 MeV [38]. The yield ratios were measured at 105°, 135°, 150°, and 165° using measurements at $\theta_{\rm lab} = 90°$ as the reference angle. Figure 18 shows the *R*-matrix fit to yield-ratio data.

D. ^{15}N(p, α_1)^{12}C

Reference [21] provides the only data available for the ^{15}N(p, α_1)^{12}C reaction channel in the energy region of interest where the α particle was detected directly. Figures 4 and 5 of Ref. [21] are difficult to digitize because of the way in which the cross sections are displayed. This translates into larger uncertainties than the error bars suggest in the regions of low

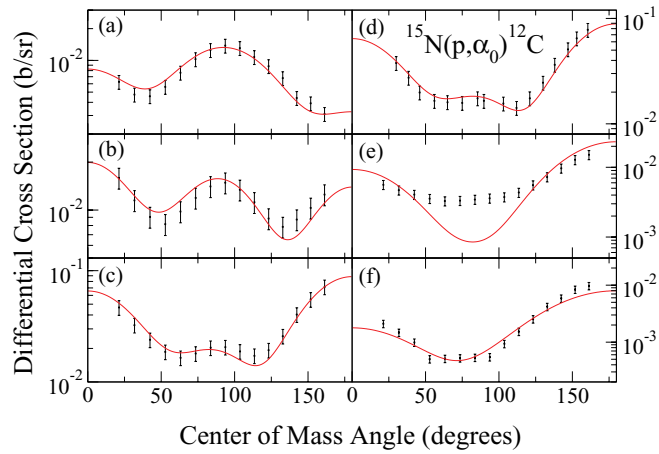

FIG. 10. (Color online) Fits to the ^{15}N(p, α_0)^{12}C angular distributions of Ref. [29] at $E_p = 1.163$, 1.188, 1.213, 1.214, 1.238, and 1.263 MeV [labeled (a) through (f), respectively].

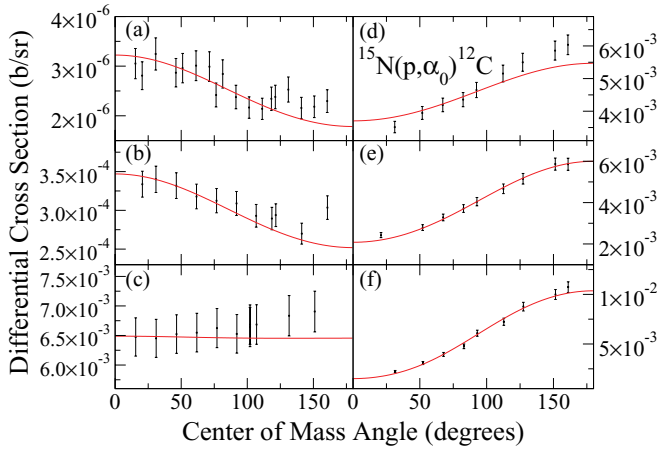

FIG. 11. (Color online) Fits to the ^{15}N$(p, \alpha_0)^{12}$C angular distributions of Ref. [31] at $E_p = 0.149$, 0.247, 0.344, 0.450, 0.600, and 0.750 MeV [labeled (a) through (f), respectively].

cross section between resonances. The angular distributions from Fig. 6 of Ref. [21] at $E_p = 1.214$ and 1.643 MeV are also included. These data sets are expected to have very limited constraint on the ^{15}N$(p, \gamma_0)^{16}$O data since only the higher energy 1^- resonance is present in the data region but is not clearly resolved. The data resolve two 3^- resonances at $E_x = 13.13$ and 13.27 MeV and a 1^+ at 13.67 MeV which are consistent with resonance states observed in other reaction channels. Fits are shown in Figs. 19 and 20.

The recent angle-integrated ^{15}N$(p, \alpha_1\gamma)^{12}$C data reported in Ref. [40] provide considerable improvement over the ^{15}N$(p, \alpha_1)^{12}$C data of Ref. [6] and cover a similar energy

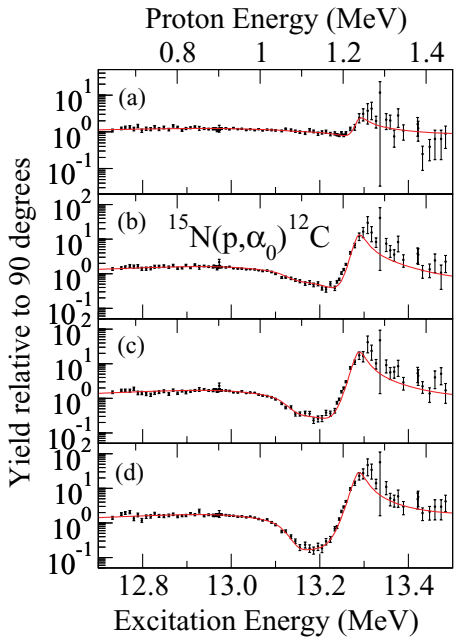

FIG. 12. (Color online) Fits to the ^{15}N$(p, \alpha_0)^{12}$C yield-ratio data of Ref. [38] at $\theta_{lab} = 105°$, 135°, 150°, and 165° [labeled (a) through (d) respectively]. Laboratory proton energy is given on the top horizontal axis and excitation energy on the bottom horizontal axis of each plot.

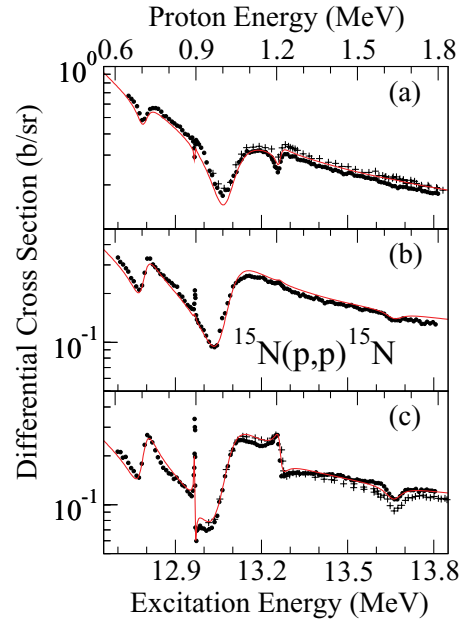

FIG. 13. (Color online) Fits to the ^{15}N$(p, p)^{15}$N cross-section data from Ref. [19] (circles) at $\theta_{lab} = 86°$, 122°, and 159° [labeled (a) through (c) respectively] and from Ref. [21] (pluses) at $\theta_{lab} = 86°$ and 159° [labeled (a) and (c) respectively]. An uncertainty of 3% has been assumed for each data point. Laboratory proton energy is given on the top horizontal axis and excitation energy on the bottom horizontal axis of each plot.

range. This data set provides constraints on Γ_{α_1} for several levels, including the $E_x = 12.45$ and 13.09 MeV levels that dominate the ^{15}N$(p, \gamma_0)^{16}$O reaction. The fit to the data is shown in Fig. 21.

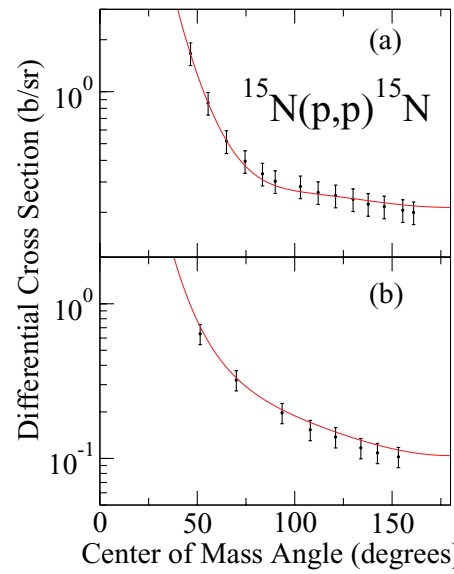

FIG. 14. (Color online) Fits to the ^{15}N$(p, p)^{15}$N angular distributions of Ref. [21] at $E_p = 1.214$ and 1.643 MeV [labeled (a) and (b), respectively].

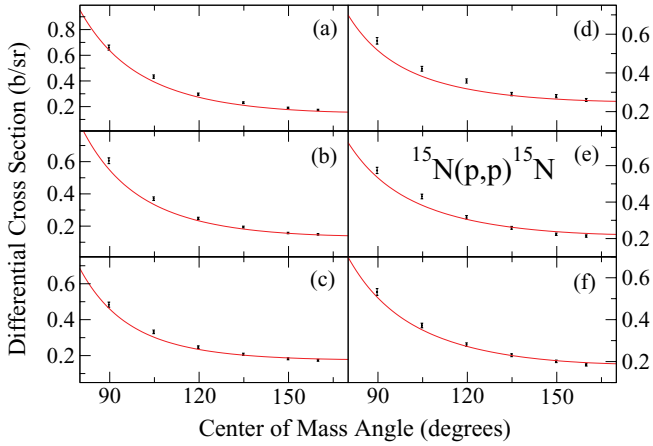

FIG. 15. (Color online) Fits to the ^{15}N(p, p)^{15}N angular distributions of Ref. [21] at E_p = 0.650, 0.675, 0.700, 0.725, 0.750, and 0.775 MeV [labeled (a) and (f), respectively].

E. ^{12}C(α, α_1)^{12}C and ^{12}C(α, p)^{15}N

Previously, the only available data set for ^{12}C(α, α_1)^{12}C and ^{12}C(α, p)^{15}N in the energy region of interest are published in Ref. [23]. The excitation curves are digitized from Fig. 2 of that work but an absolute scaling was not reported. The data sets cover the energy range over the highest-energy 1^- state in the ^{15}N(p, γ_0)^{16}O data. Also present are significant contributions from states at E_x = 12.95 (2^+), 13.13 (3^-), and 13.27 (3^-) MeV. Fits are shown in Figs. 22 and 23.

Recently, new yield-ratio data for the reactions ^{12}C(α, α_1)^{12}C and ^{12}C(α, p)^{15}N have been presented in Ref. [39]. The data are in the form of yield ratios where the ^{12}C(α, α_0)^{12}C yields measured at an angle at $\theta_{\rm lab}$ = 58.9° are used as the reference data. Experimental details can be found in Refs. [15,39,48]. The fits are presented in Figs. 24–29.

F. ^{12}C(α, α_0)^{12}C

There have been several measurements of the α-scattering cross section over the energy range above the α separation energy S_α up to the proton separation energy S_p but the data of Ref. [15] are clearly the most extensive. Data points in the vicinity of narrow resonances are removed for this analysis. Differential cross-section data for all 32 angles are included in the fit. Level parameters from the fit are in excellent agreement with those reported in Ref. [15]. The interference structures in the data, associated with resonance states at E_x = 9.59 (1^-), 10.36 (4^+), 11.50 (3^-), and 11.51 (2^+) MeV,

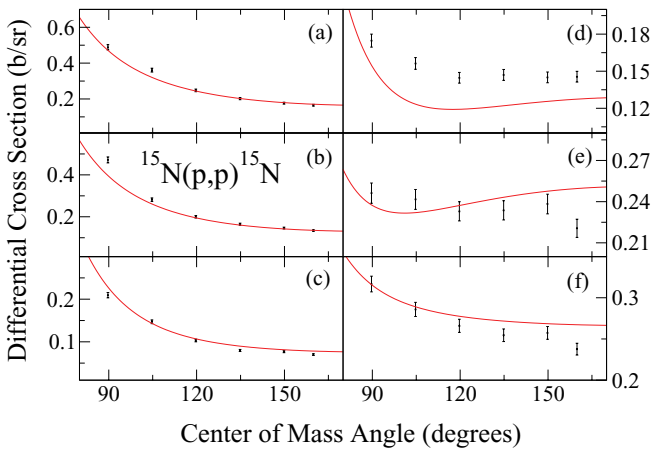

FIG. 16. (Color online) Fits to the ^{15}N(p, p)^{15}N angular distributions of Ref. [21] at E_p = 0.80, 0.85, 0.95, 1.00, 1.05, and 1.10 MeV [labeled (a) and (f) respectively].

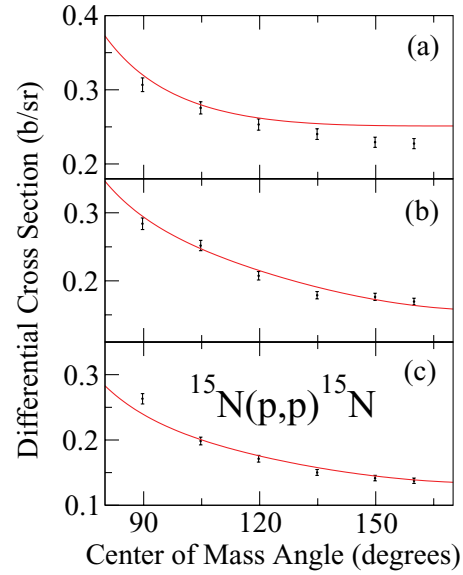

FIG. 17. (Color online) Fits to the ^{15}N(p, p)^{15}N angular distributions of Ref. [21] at E_p = 1.15, 1.30, and 1.50 MeV [labeled (a) and (c) respectively].

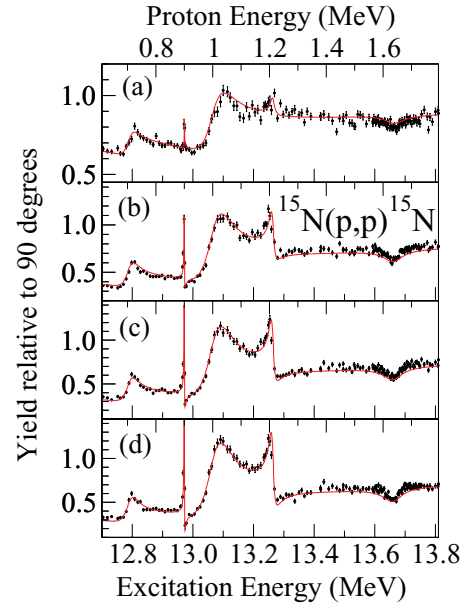

FIG. 18. (Color online) Fits to the ^{15}N(p, p)^{15}N yield-ratio data of Ref. [38] at $\theta_{\rm lab}$ = 105°, 135°, 150°, and 165° [labeled (a) through (d), respectively]. Laboratory proton energy is given on the top horizontal axis and excitation energy on the bottom horizontal axis of each plot.

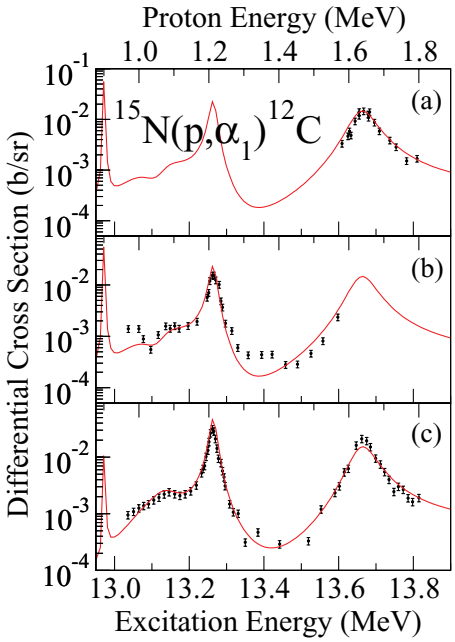

FIG. 19. (Color online) Fits to the ^{15}N$(p, \alpha_1)^{12}$C differential cross sections of Ref. [21] at $\theta_{\rm lab} = 86.2°$, 90°, and 159.5° [labeled (a), (b), and (c) respectively]. Laboratory proton energy is given on the top horizontal axis and excitation energy on the bottom horizontal axis of each plot.

are well reproduced by the *R*-matrix fit. It was critical to include a number of significant background poles of natural parity for ($l = 0$ to 5) to achieve the overall fit quality. This seems physically reasonable considering the number of broad resonances present at higher energy (e.g., Refs. [11,14]).

The best quality α-scattering cross-section data above S_p are the ones shown in Fig. 6 of Ref. [24]. The excitation curve data are available, in tabulated form, in the original thesis [53]. Angular distribution data from Ref. [24] are not available in the thesis and are obtained from EXFOR [51]. The angular distributions are found to be in good agreement with the excitation curve data if normalization corrections (maximum of ±20%) are applied (see Table XI of Appendix B). This is likely the result of the digitization process as the figure is quite difficult to scan. The states included in the fitting of this

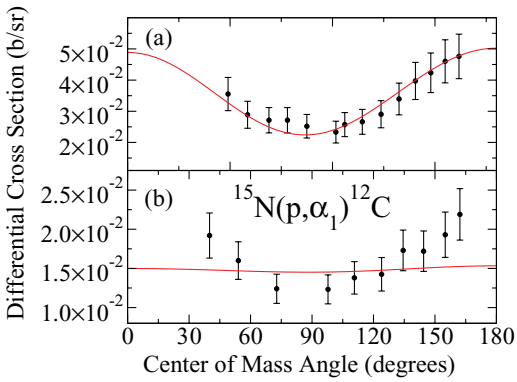

FIG. 20. (Color online) Fit to the ^{15}N$(p, \alpha_1)^{12}$C angular distribution of Ref. [21] at $E_p = 1.214$ MeV.

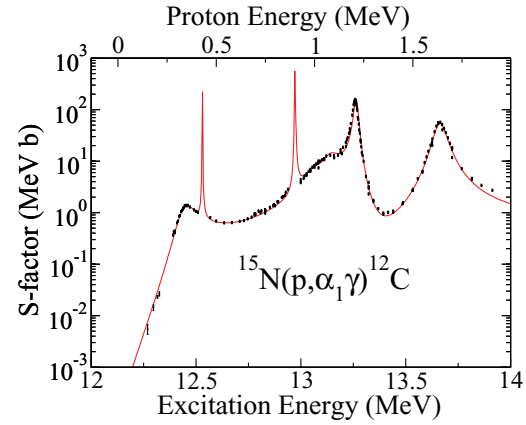

FIG. 21. (Color online) Fit to the ^{15}N$(p, \alpha_1\gamma_1)^{12}$C angle-integrated cross-section data of Ref. [10]. Laboratory proton energy is given on the top horizontal axis and excitation energy on the bottom horizontal axis of each plot.

data are the two 1^- resonances observed in the ^{15}N$(p, \gamma_0)^{16}$O data as well as states at $E_x = 12.95$ (2^+), 13.13 (3^-), 13.27 (3^-), and 13.85 (4^+) MeV and the tail of the broad state at $E_x = 14.52$ (5^-) MeV. Fits are shown in Figs. 30, 31, 32, and 33.

The single excitation curve at $\theta_{\rm lab} = 165°$ from Ref. [33] covers the excitation energy region from nearly S_α to just above the energy region covered by Ref. [24]. While less extensive than the data from Ref. [24], this data set was quite useful because it resolves a 4^+ resonance at $E_x = 13.85$ MeV and the tail contribution from a broad 5^- resonance at energies just above the energy region covered by Ref. [24]. The contribution from the 5^- resonance was especially significant in fitting the data of Ref. [24]. Fits are shown in Figs. 34–39. Phase shifts ($l = 0$ to 5) from Ref. [27], shown in Fig. 40, were also included in an effort to add further constraint at higher energy.

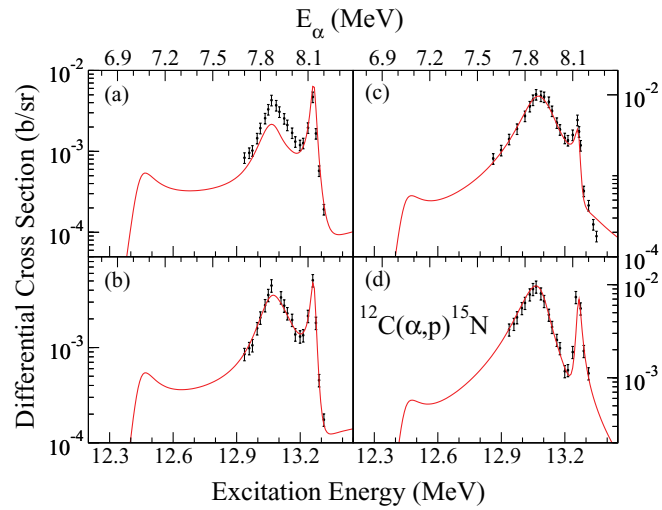

FIG. 22. (Color online) Fits to the ^{12}C$(\alpha, p)^{15}$N differential cross sections of Ref. [52] at $\theta_{\rm lab} = 30°$, 40°, 90°, and 120° [labeled (a) through (d), respectively]. Laboratory α-particle energy is given on the top horizontal axis and excitation energy on the bottom horizontal axis of each plot.

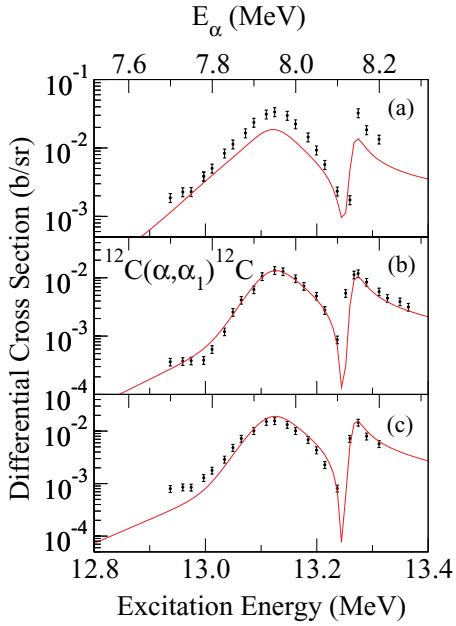

FIG. 23. (Color online) Fits to the ^{12}C$(\alpha, \alpha_1)^{12}$C differential cross sections of Ref. [52] at $\theta_{\rm lab} = 40^\circ$, 90°, and 120° [labeled (a) through (d), respectively]. Laboratory α-particle energy is given on the top horizontal axis and excitation energy on the bottom horizontal axis of each plot.

In addition, yield-ratio data have recently been reported in Ref. [39] which cover a similar energy range as in Ref. [24] and are found to be in excellent agreement. The yield-ratio data are analyzed using the same technique used previously [15,48] by taking the ratio of the yields to a given reference angle. The fits are shown in Figs. 41–44.

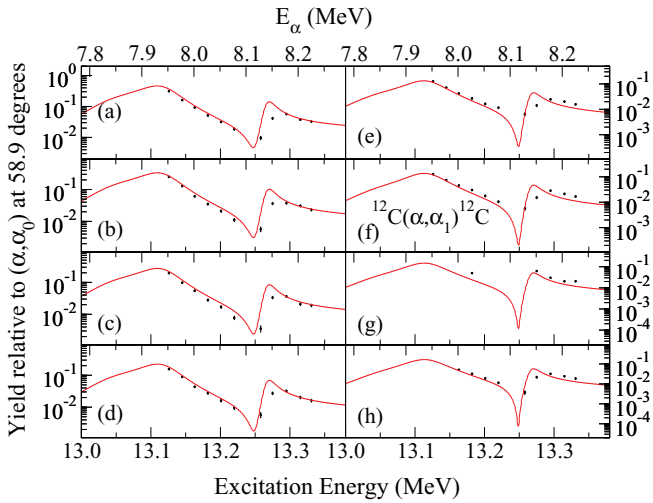

FIG. 24. (Color online) Fits to the ^{12}C$(\alpha, \alpha_1)^{12}$C differential yields of Ref. [39] at $\theta_{\rm lab} = 24.0^\circ$, 33.9°, 38.9°, 43.9°, 63.9°, 68.9°, 74.0°, and 79.0° [labeled (a) through (h), respectively]. The (α, α_1) yields were divided by the corresponding (a, a_0) yields. Laboratory α-particle energy is given on the top horizontal axis and excitation energy on the bottom horizontal axis of each plot.

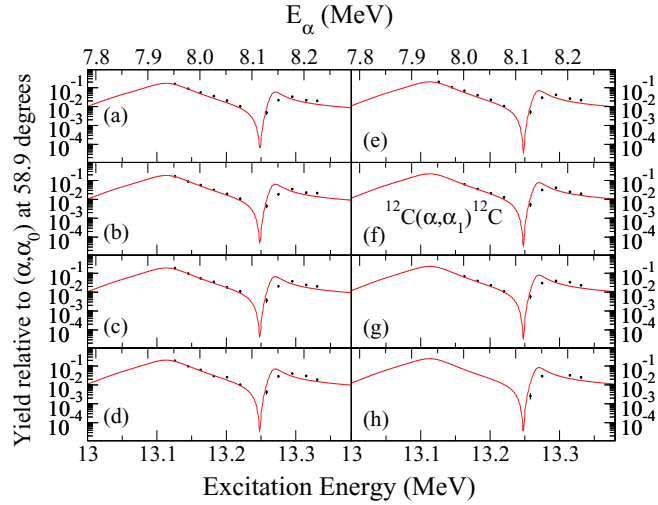

FIG. 25. (Color online) Fits to the ^{12}C$(\alpha, \alpha_1)^{12}$C differential yields of Ref. [39] at $\theta_{\rm lab} = 80.8^\circ$, 84.0°, 85.8°, 89.0°, 90.8°, 94.0°, 95.8°, and 99.0° [labeled (a) through (h), respectively]. The (α, α_1) yields were divided by the corresponding (a, a_0) yields. Laboratory α-particle energy is given on the top horizontal axis and excitation energy on the bottom horizontal axis of each plot.

G. ^{12}C$(\alpha, \gamma)^{16}$O

The ^{12}C$(\alpha, \gamma)^{16}$O reaction is of particular relevance for the synthesis of the elements in stellar helium burning since it determines the ^{12}C/^{16}O ratio in our universe, a ratio that affects not only late stellar evolution but also the physics of white dwarf and type Ia supernovae explosions. The low-energy cross section of the reaction is characterized by the interference between the tails of broad resonances and subthreshold states as well as direct capture components. There exist a wealth of experimental data taken to explore the low-energy cross

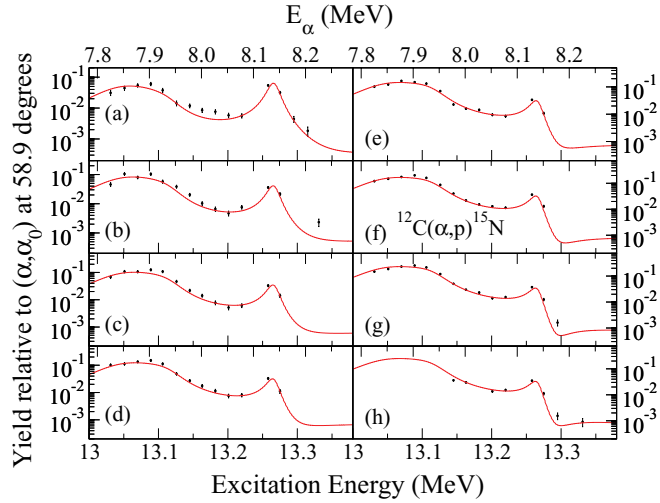

FIG. 26. (Color online) Fits to the ^{12}C$(\alpha, p)^{12}$C differential yields of Ref. [39] at $\theta_{\rm lab} = 24.0^\circ$, 33.9°, 38.9°, 43.9°, 48.9°, 54.0°, 68.9°, and 74.0° [labeled (a) through (h), respectively]. The (α, p) yields were divided by the corresponding (a, a_0) yields. Laboratory α-particle energy is given on the top horizontal axis and excitation energy on the bottom horizontal axis of each plot.

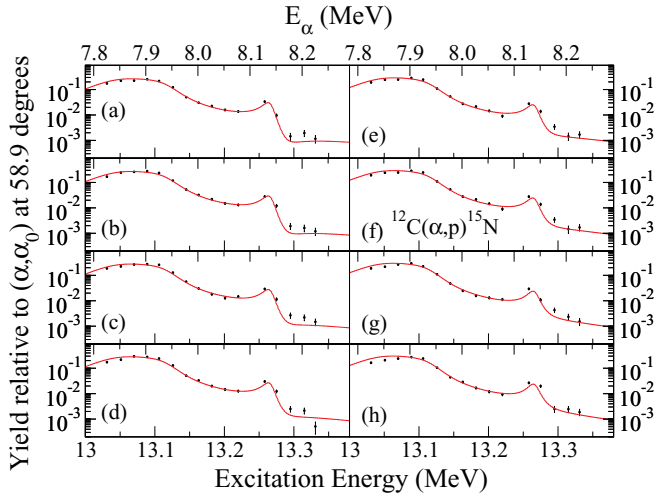

FIG. 27. (Color online) Fits to the ^{12}C(α, p)^{12}C differential yields of Ref. [39] at $\theta_{\rm lab} = 79.0^\circ$, 80.8°, 84.0°, 85.8°, 89.0°, 90.8°, 94.0°, and 95.8° [labeled (a) through (h), respectively]. The (α, p) yields were divided by the corresponding (a, a_0) yields. Laboratory α-particle energy is given on the top horizontal axis and excitation energy on the bottom horizontal axis of each plot.

section of the reaction and to determine a reliable reaction rate for stellar temperature conditions by R matrix or other theoretical extrapolation techniques [54]. While the analysis of the ^{12}C(α,γ)^{16}O reaction is not the primary goal of this paper, the high-energy data covering the excitation range approaching the proton separation energy S_p in ^{16}O are relevant for the ^{15}N + p reaction system.

For the energy range of the ^{12}C(α,γ)^{16}O channel approaching the proton separation energy, the data from Refs. [16,37] are of particular interest. The data, summarized in Table I of Ref. [16], were measured using the inverse kinematics technique where the ^{16}O recoil was separated and detected using the ERNA recoil separator. Using this technique, the ^{12}C(α,γ)^{16}O cross section represents the sum over all possible γ-decay channels. In addition, cascade transition data to all of the bound states of ^{16}O have been reported in Ref. [37] but covering a more limited energy range.

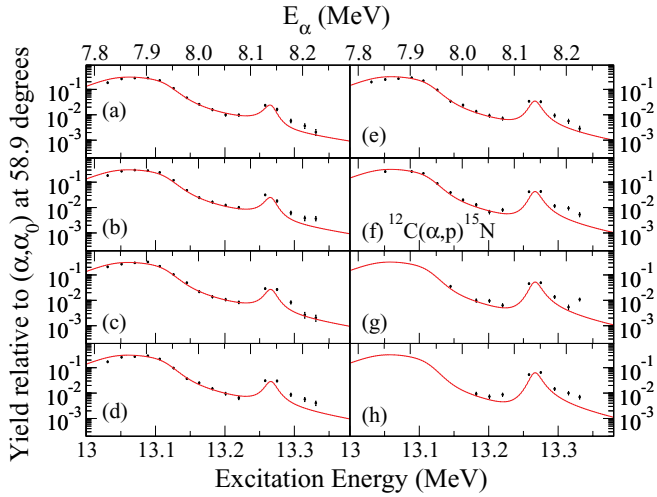

FIG. 28. (Color online) Fits to the ^{12}C(α, p)^{12}C differential yields of Ref. [39] at $\theta_{\rm lab} = 99.0^\circ$, 100.8°, 103.9°, 105.8°, 110.8°, 115.8°, 120.8°, and 125.8° [labeled (a) through (h), respectively]. The (α, p) yields were divided by the corresponding (a, a_0) yields. Laboratory α-particle energy is given on the top horizontal axis and excitation energy on the bottom horizontal axis of each plot.

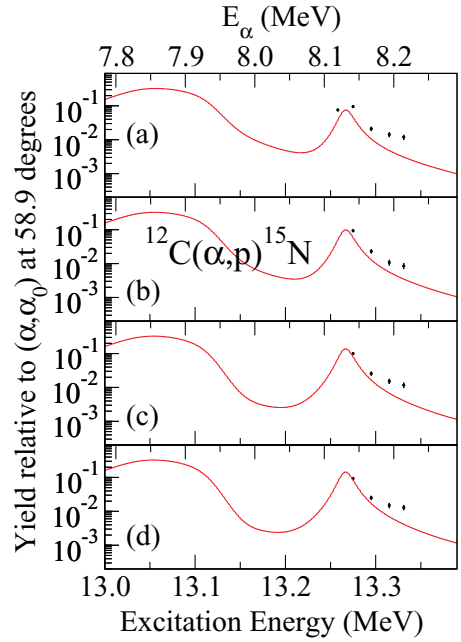

FIG. 29. (Color online) Fits to the ^{12}C(α, p)^{12}C differential yields of Ref. [39] at $\theta_{\rm lab} = 130.8^\circ$, 140.8°, 150.8°, and 160.8° [labeled (a) through (c), respectively]. The (α, p) yields were divided by the corresponding (a, a_0) yields. Laboratory α-particle energy is given on the top horizontal axis and excitation energy on the bottom horizontal axis of each plot.

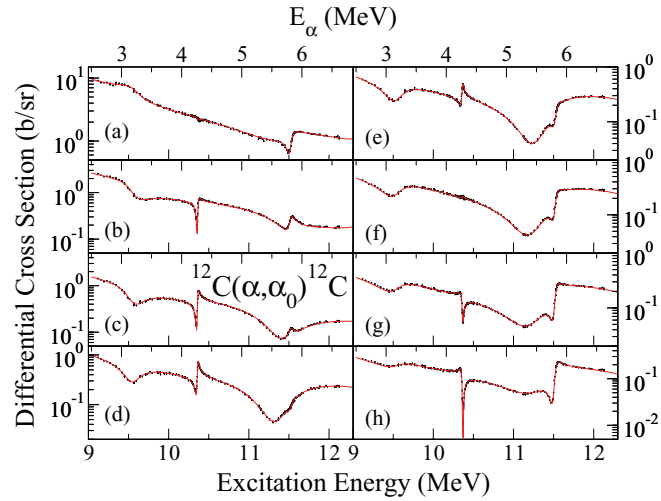

FIG. 30. (Color online) Fits to the ^{12}C(α, α_0)^{12}C differential cross-section data of Ref. [15] at $\theta_{\rm lab} = 24^\circ$, 33.9°, 38.9°, 43.9°, 48.9°, 54.0°, 58.9°, and 63.9° [labeled (a) through (h), respectively]. Laboratory α-particle energy is given on the top horizontal axis and excitation energy on the bottom horizontal axis of each plot.

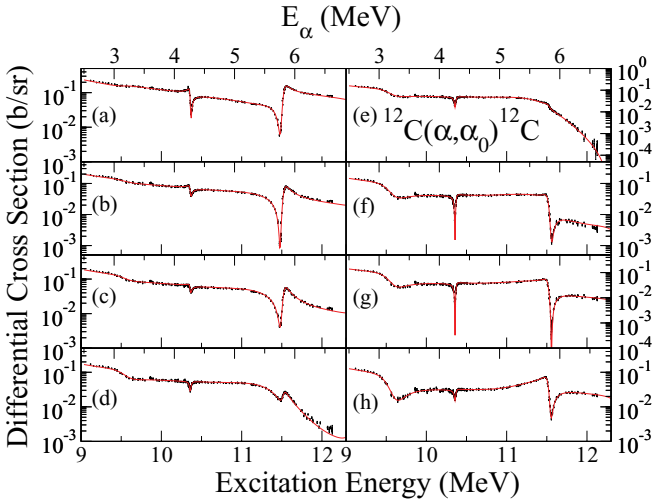

FIG. 31. (Color online) Fits to the ^{12}C$(\alpha, \alpha_0)^{12}$C differential cross-section data of Ref. [15] at $\theta_{\rm lab} = 68.9°$, 74.0°, 75.8°, 79°, 80.8°, 84.0°, 85.8°, and 89.0° [labeled (a) through (h), respectively]. Laboratory α-particle energy is given on the top horizontal axis and excitation energy on the bottom horizontal axis of each plot.

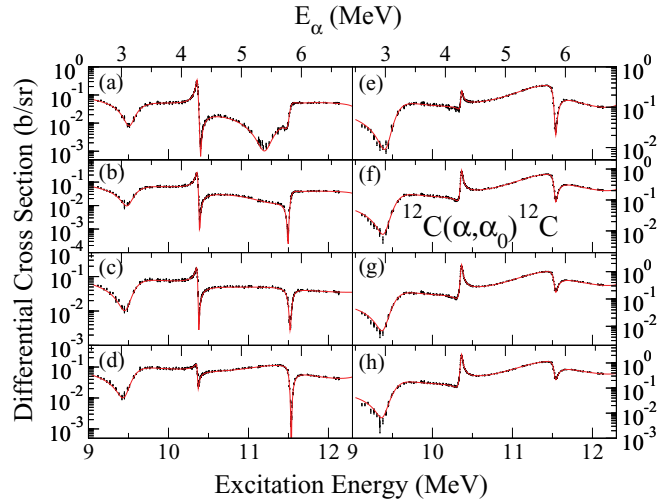

FIG. 33. (Color online) Fits to the ^{12}C$(\alpha, \alpha_0)^{12}$C differential cross-section data of Ref. [15] at $\theta_{\rm lab} = 115.8°$, 120.8°, 125.8°, 130.8°, 140.8°, 150.8°, 160.8°, and 165.9° [labeled (a) through (h) respectively]. Laboratory α-particle energy is given on the top horizontal axis and excitation energy on the bottom horizontal axis of each plot.

In Ref. [16], the data are compared to an *R*-matrix calculation from Ref. [55]. This comparison displays substantial discrepancies between the calculation and the data in the regions between resonances (see Fig. 3 of that work), in particular, the region between the broad 4^+ ($E_x = 10.36$ MeV) and 2^+ ($E_x = 11.51$ MeV) resonances. This clearly indicates the existence of at least one additional reaction component.

Figure 45 shows the fit to the ^{12}C$(\alpha,\gamma)^{16}$O data of Refs. [16,37]. The cascade transitions data reveal several previously unobserved components to the cross section from direct capture contributions through the $E_x = 6.05$ and 6.13 MeV bound states and several γ-ray cascade transitions from the 3^- and 2^+ unbound states at $E_x = 11.49$ and 11.51 MeV, respectively, which were not previously considered in Ref. [55] but have been noted elsewhere [56,57]. The calculation shown here demonstrates how the previous discrepancies can be accounted for by these additional contributions. In the current analysis, the values of many of the partial widths and the α-particle ANCs have been fixed to either previously determined values or those determined though a preliminary analysis. Since the analysis at energies below the proton separation energy is only preliminary, no uncertainties are reported for these fit parameters. Likewise, Fig. 45 does not include an

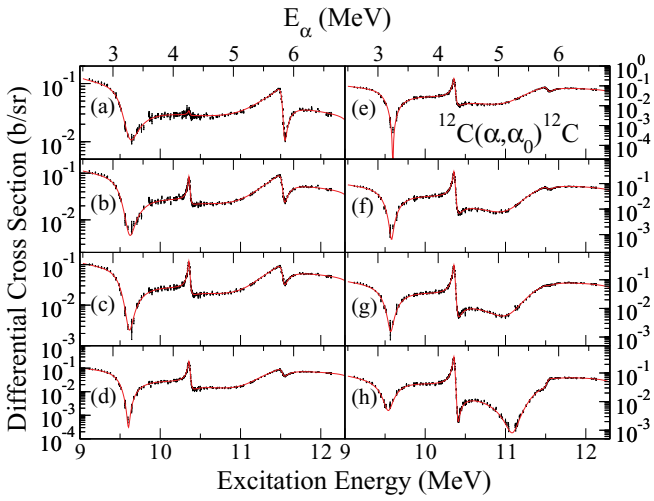

FIG. 32. (Color online) Fits to the ^{12}C$(\alpha, \alpha_0)^{12}$C differential cross-section data of Ref. [15] at $\theta_{\rm lab} = 90.8°$, 94.0°, 95.8°, 99.0°, 100.8°, 103.9°, 105.8°, and 110.8° [labeled (a) through (h), respectively]. Laboratory α-particle energy is given on the top horizontal axis and excitation energy on the bottom horizontal axis of each plot.

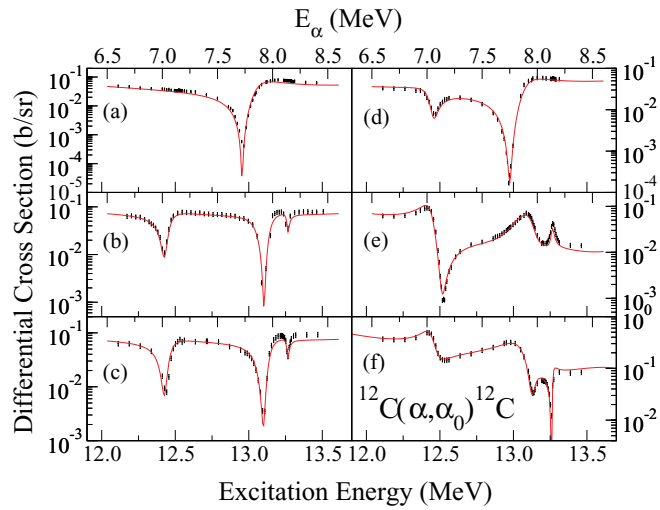

FIG. 34. (Color online) Fits to the ^{12}C$(\alpha, \alpha_0)^{12}$C differential cross-section data of Ref. [24] at $\theta_{\rm lab} = 71.55°$, 104.5°, 106.6°, 124.89°, 136.06°, and 167° [labeled (a) through (f) respectively]. Laboratory α-particle energy is given on the top horizontal axis and excitation energy on the bottom horizontal axis of each plot.

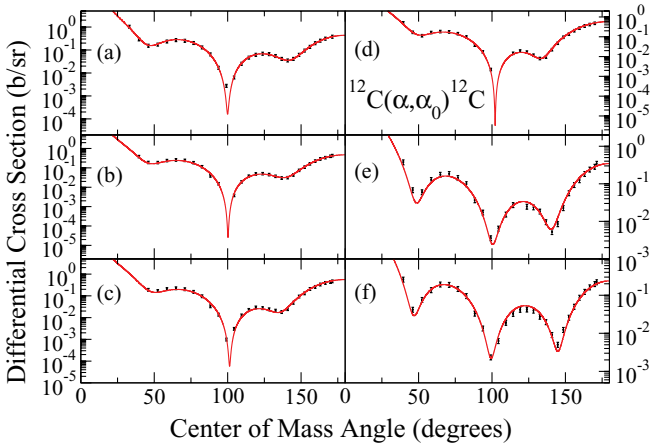

FIG. 35. (Color online) Fits to the $^{12}C(\alpha,\alpha_0)^{12}C$ angular distribution data of Ref. [24] at $E_\alpha = 6.600$, 6.885, 6.965, 6.99, 7.064, and 7.093 MeV [labeled (a) through (f), respectively].

extrapolation of the $^{12}C(\alpha,\gamma)^{16}O$ data to low energy. This will be the subject of a future publication.

Several experimental examinations have been made of the $^{12}C(\alpha,\gamma_0)^{16}O$ cross section near the two 1^- levels just above S_p which are included in the present analysis [22,25,26,28]. The $\theta_{lab} = 90^\circ$ differential yield data from Ref. [28] could be read directly from Table V of that work. The other excitation curves had to be digitized from the figures of the given work: Reference [26] from Fig. 3, Ref. [25] from Fig. 6, and Ref. [22] from Fig. 3. The excitation curves show reasonable consistency in the shape of the excitation curves, but the overall normalizations are not available for much of the data. For this analysis, the absolute cross-section scale was determined by the angle-integrated data of Ref. [26]. This is further discussed in Sec. VI and the normalizations are given in Table XI of Appendix B.

Asymmetries in $^{12}C(\alpha,\gamma_0)^{16}O$ angular distribution data in this region also point to a contribution from a broad positive parity level. The 2^+ level located at $E_x = 12.95$ MeV was a natural candidate. To constrain a fit of the $E2$ ground-state

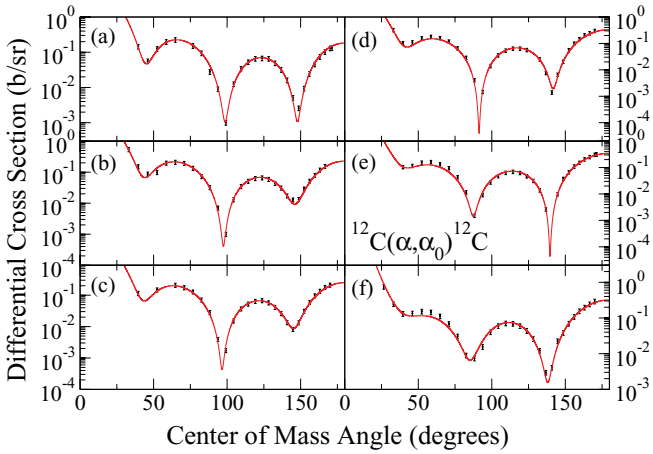

FIG. 36. (Color online) Fits to the $^{12}C(\alpha,\alpha_0)^{12}C$ angular distribution data of Ref. [24] at $E_\alpha = 7.167$, 7.400, 7.500, 7.700, 7.767, and 7.800 MeV [labeled (a) through (f) respectively].

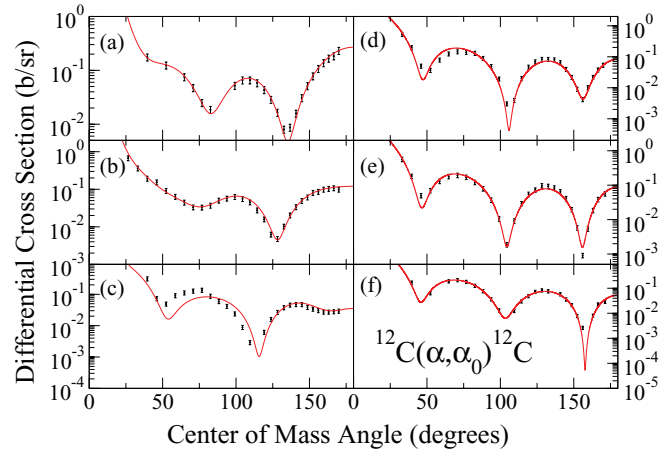

FIG. 37. (Color online) Fits to the $^{12}C(\alpha,\alpha_0)^{12}C$ angular distribution data of Ref. [24] at $E_\alpha = 7.845$, 7.900, 7.960, 8.015, 8.050, and 8.113 MeV [labeled (a) through (f) respectively].

transition, the differential yield curves at $\theta_{lab} = 61^\circ$, 90°, and 135° as well as angular distributions at $E_\alpha = 7.7$, 7.88, and 8.1 MeV from Ref. [25] (from Fig. 7) and at $E_\alpha = 7.06$, 7.42, 7.88, and 8.0 MeV from Ref. [22] (Fig. 4) are included. The data are found to be consistent with a value of $\Gamma_{\gamma_0} = 0.7(2)$ eV for the 2^+ level reported in Ref. [17] but a lack of absolute measurements for the data makes the constraint rather weak. The fitted data are shown in Figs. 46 and 47.

VI. DISCUSSION

The many different data sets of the various reaction channels are found to be remarkably consistent considering the diversity and amount of data considered (see Table I). The R-matrix fit is able to reproduce the data very well in most instances. The largest sources of inconsistencies in the fitting arise from the approximation of thin target yields and a likely incomplete description of the cross section at the highest energies. The

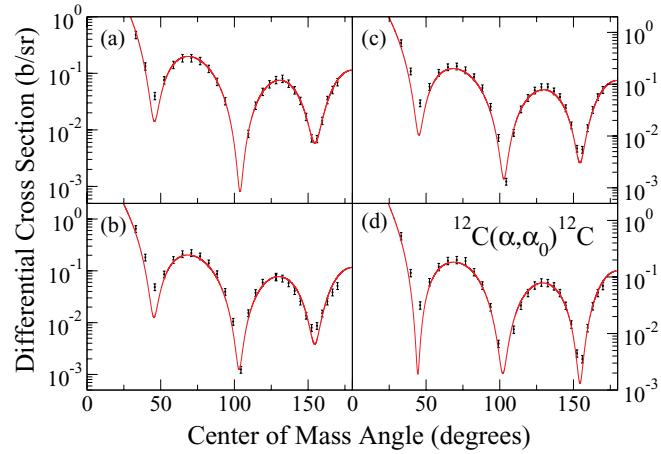

FIG. 38. (Color online) Fits to the $^{12}C(\alpha,\alpha_0)^{12}C$ angular distribution data of Ref. [24] at $E_\alpha = 8.196$, 8.247, 8.300, and 8.500 MeV [labeled (a) through (d) respectively].

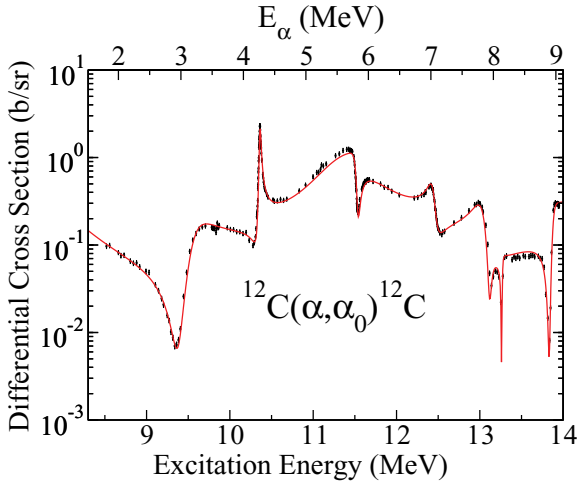

FIG. 39. (Color online) Fits to the ^{12}C$(\alpha, \alpha_0)^{12}$C differential cross-section data of Ref. [33] at $\theta_{\rm lab} = 165°$). Laboratory α-particle energy is given on the top horizontal axis and excitation energy on the bottom horizontal axis of the plot.

specific cases where these discrepancies occur are highlighted here.

In general, the thin target yield approximation holds well for the given analysis because nearly all of the levels considered have total widths in excess of the typical target thicknesses

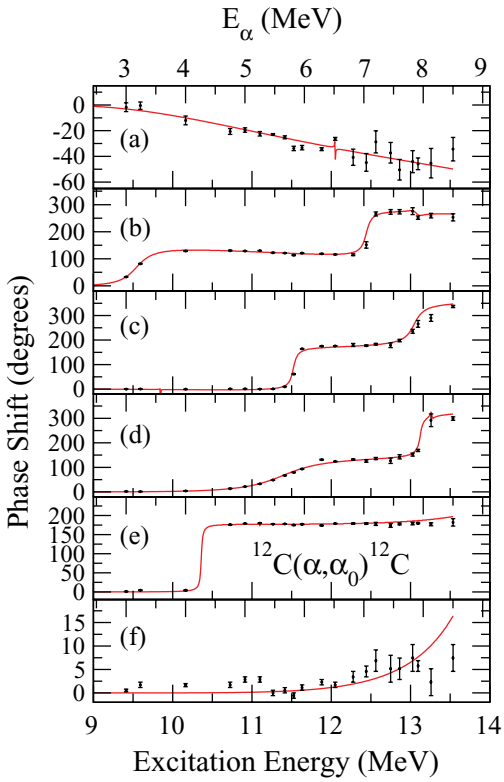

FIG. 40. (Color online) Fits to the phase shifts from Ref. [27] for $l = 0$, 1, 2, 3, 4, and 5 [labeled (a) through (f) respectively] included in the *R*-matrix analysis. Laboratory α-particle energy is given on the top horizontal axis and excitation energy on the bottom horizontal axis of each plot.

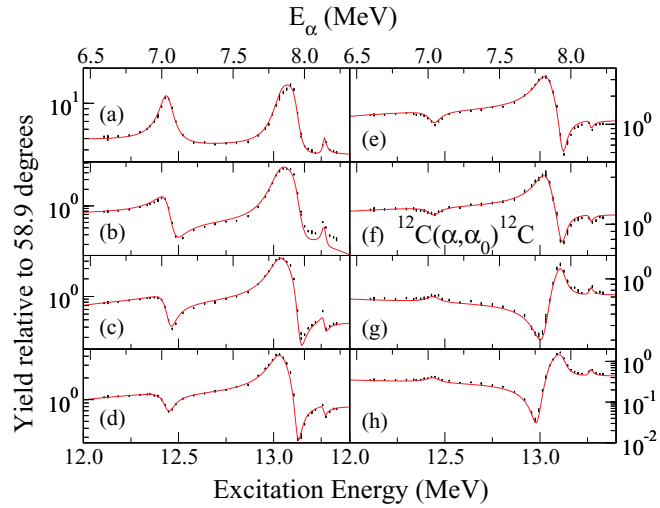

FIG. 41. (Color online) Fits to the ^{12}C$(\alpha, \alpha_0)^{12}$C yield data of Ref. [39] at $\theta_{\rm lab} = 24.0°$, 33.9°, 38.9°, 43.9°, 48.9°, 54.0°, 63.9°, and 68.9° [labeled (a) through (h) respectively]. Laboratory α-particle energy is given on the top horizontal axis and excitation energy on the bottom horizontal axis of each plot.

used in the experimental measurements. The structure of ^{16}O facilitates this as most levels clearly fall into either a narrow or broad resonance category. Two levels which are fit in this analysis have total widths which fall somewhere in between. These are the levels at $E_x = 12.97$ (2^-) and 13.26 (3^-) MeV. While the 2^- level is quite narrow, $\Gamma_{\rm total} <$ 2 keV, its unnatural parity limits it to only the ^{15}N$(p, p)^{15}$N and ^{15}N$(p, \alpha_1)^{12}$C reactions. The resonance is included in the analysis, but its level parameters were fixed to those found in the literature [17]. The 3^- level, being of natural parity, can be populated in all reaction channels and is observed in all data sets which cover this energy range. This level

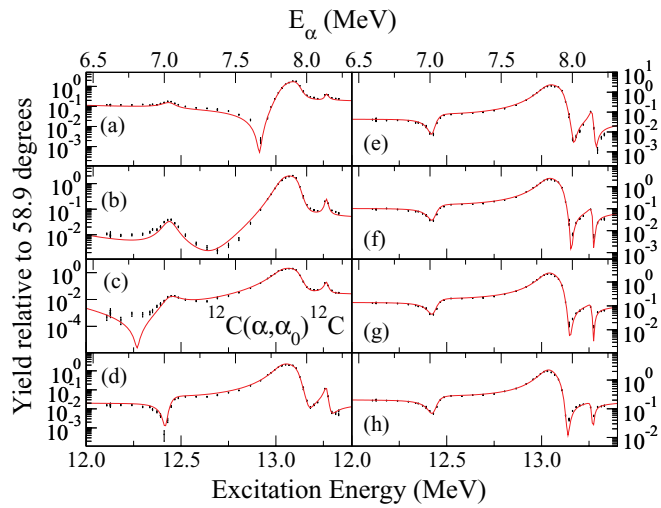

FIG. 42. (Color online) Fits to the ^{12}C$(\alpha, \alpha_0)^{12}$C yield data of Ref. [39] at $\theta_{\rm lab} = 74.0°$, 75.8°, 80.8°, 84.0°, 85.8°, 89.0°, 90.8°, and 94.0° [labeled (a) through (h), respectively]. Laboratory α-particle energy is given on the top horizontal axis and excitation energy on the bottom horizontal axis of each plot.

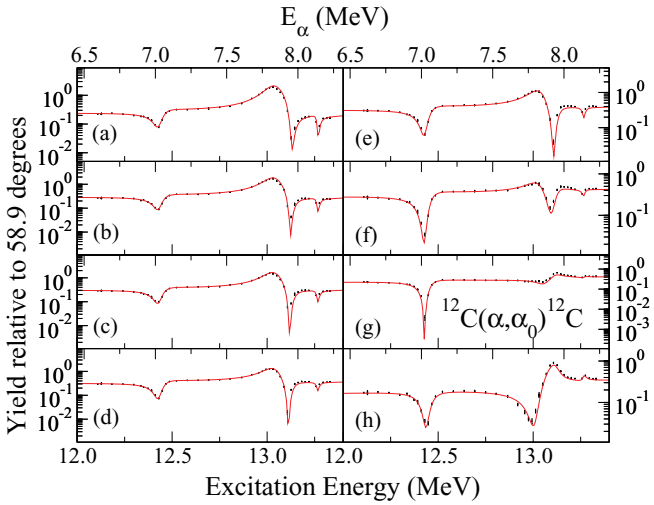

FIG. 43. (Color online) Fits to the $^{12}C(\alpha,\alpha_0)^{12}C$ yield data of Ref. [39] at $\theta_{lab} = 95.8°$, 99.0°, 100.8°, 103.9°, 105.8°, 110.8°, 115.8°, and 120.8° [labeled (a) through (h) respectively]. Laboratory α-particle energy is given on the top horizontal axis and excitation energy on the bottom horizontal axis of each plot.

has a total width of $\Gamma_{total} \approx 25$ keV, very close to the target thickness for many of the experiments considered. Because the experimental measurements are performed with a variety of targets with different thicknesses, inconsistencies appear in the *R*-matrix fit in the regions of these resonances. These inconsistencies manifest as both apparent shifts in resonance energy and resonance shape. Target integration tests, i.e., the integration of the cross section over effective energy thickness of the target, showed that these deviations are consistent with target thickness effects. The global fit does not include these corrections at this time as target integration calculations are too demanding in computing time to be practical. The energy

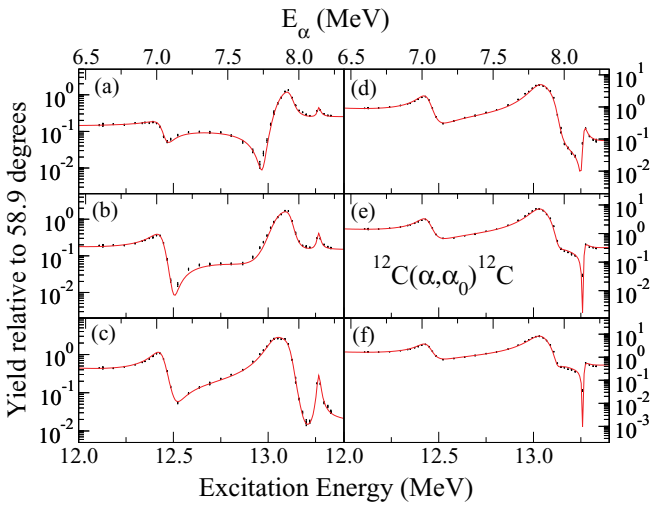

FIG. 44. (Color online) Fits to the $^{12}C(\alpha,\alpha_0)^{12}C$ yield data of Ref. [39] at $\theta_{lab} = 125.8°$, 130.8°, 140.8°, 150.8°, 160.8°, and 165.9° [labeled (a) through (f), respectively]. Laboratory α-particle energy is given on the top horizontal axis and excitation energy on the bottom horizontal axis of each plot.

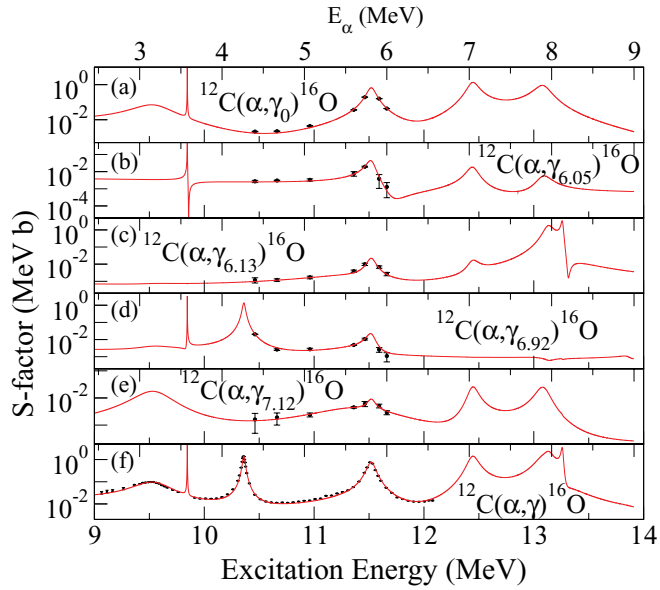

FIG. 45. (Color online) Fits to the angle-integrated cross section $^{12}C(\alpha,\gamma)^{16}O$ of Refs. [16,37] for the ground state and 6.049-, 6.130-, 6.917-, and 7.117-MeV transitions and for the total capture cross section [labeled (a) through (f), respectively]. At energies above the proton separation energy, the cross section is determined by other available reaction-channel measurements. Laboratory α-particle energy is given on the top horizontal axis and excitation energy on the bottom horizontal axis of each plot.

for the 3^- level at $E_x = 13.26$ MeV is fixed at the central value determined from the $^{15}N(p,\alpha_1\gamma)^{12}C$ data where the resonance is most clearly defined. The partial widths of the level are allowed to vary freely in the fit, and despite the neglect of target effects, the fit results in values which are in reasonable agreement with those previously reported.

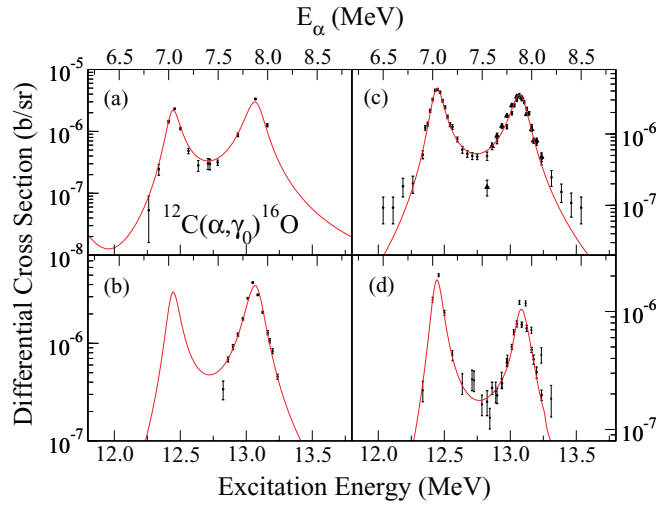

FIG. 46. (Color online) Fits to the $^{12}C(\alpha,\gamma_0)^{16}O$ differential cross-section data at 45° (Ref. [22]), 61° (Ref. [25]), 90° (Refs. [25,28]), and 135° (Ref. [25]) [labeled (a) through (d) respectively]. Laboratory α-particle energy is given on the top horizontal axis and excitation energy on the bottom horizontal axis of each plot.

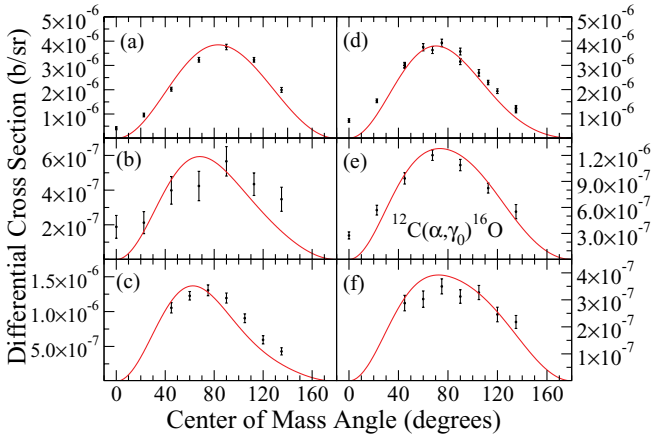

FIG. 47. (Color online) Fits to the ^{12}C(α, γ_0)^{16}O angular distribution data of Refs. [22,25] at E_α = 7.06, 7.42, 7.70, 7.88, 8.00, and 8.10 MeV [labeled (a) through (f), respectively].

The largest deviation of the *R*-matrix fit from the data over all the reaction channels was observed at the highest energies considered ($E_x > 13$ MeV). This can be partly explained by target effects in the vicinity of the narrow 3^- level but is also likely the result of the interference of broad resonance contributions. In Ref. [14], it was observed via ^{12}C(α, α_0)^{12}C that in the excitation energy region from 13.5 to 15.0 MeV several broad resonance structures dominate the cross section. Ideally, the *R*-matrix fit would be extended to higher energies in order to better ensure that effects from these broad states are properly included. However, in both Refs. [14] and [58], relatively poor *R*-matrix fits are achieved. An *R*-matrix fit was attempted over this energy region in the current analysis but fits of reasonable quality could not be obtained with the six levels reported in Ref. [58] [E_x = 13.8 (4^+), 14.0 (0^+), 14.2 (3^-), 14.6 (4^+), 14.6 (5^-), and 14.8 (6^+)]. The 4^+ at 13.8 MeV is included in the current analysis and is visible as the highest-energy resonance in the ^{12}C(α, α_0)^{15}N data of Ref. [33]. As the lowest-energy 6^+ resonance in ^{16}O, the resonance at 14.8 MeV is well studied (e.g., Ref. [59]). The remaining three resonances are thought to be quite broad ($\Gamma >$ 0.5 MeV) but their widths and spin-parties remain uncertain. Because of the difficulty in fitting the data of Ref. [14], the tail contributions for these broad resonance are described by background poles at higher energy. The assumption of the background pole contribution is that it represents the sum of all higher-energy resonances with their interferences averaged. This may be a rather poor approximation in this energy region because the large α-cluster structure of ^{16}O at higher energies (e.g. Ref. [11]) likely results in asymmetric interference over a relatively broad energy ranges. A successful description of the higher-energy data may be necessary for an improved fitting at the highest energies considered in the work.

Several tests were performed to check the sensitivity of the fit to contributions from background poles of differing spin-party in all the reaction channels. Only pole contributions which significantly improved the χ^2 of the fit were retained. In general, the background poles were critical for fitting the ^{12}C(α, α_0)^{12}C (see Sec. V F) and ^{15}N(p, γ_0)^{16}O (see Sec. VI B) data but were less important for the other reactions.

Besides the two general difficulties discussed above, there are a few problems encountered with specific data sets. The shape of the ^{12}C(α, γ_0)^{16}O data from Ref. [28] shows good agreement near the resonances but deviates substantially in the nonresonant regions. From comparison to other data [22,25,26], it seems likely that this discrepancy is from background contributions that were not accurately subtracted from the very low yield data points. Further, the absolute scale of the data from Ref. [28] had to be multiplied by a factor of 2 in order to be compatible with the *R*-matrix calculation. The partial widths are well constrained by the much higher-quality ^{15}N(p, γ_0)^{16}O and ^{12}C(α, α_0)^{12}C data. The angle-integrated cross-section data from Ref. [26] is in good agreement with the ^{15}N(p, γ_0)^{16}O data in both absolute scale and shape but required a correction of ∼25 keV down in energy. The remaining data from Refs. [25] and [22] showed good agreement in the shape of the excitation curves but since no absolute cross-section scale was reported, these excitation curves and angular distributions are scaled to match the calculation greatly decreasing their constraint on the overall fit. The normalization factors are given in Table XI of Appendix B.

Deviation from the fit was also observed in the angular distribution data at $E_\alpha = 7.960$ of Ref. [24], shown in Fig. 37(c). The fit of Ref. [24], shown in Fig. 5 of that work, also shows a similar deviation between fit and data. Nearby angular distributions at $E_\alpha = 7.9$ and 8.015 MeV show good agreement with the *R*-matrix fit. The reason for the inconsistency with this angular distribution data remains unknown.

Additionally, the angular distribution at $E_p = 1.238$ MeV from the data of Ref. [29] is found to be inconsistent with the fit. This angular distribution lies on the high-energy side of the 3^- resonance at $E_x = 13.26$ MeV ($E_p = 1.208$ MeV). It varies substantially from the calculation while the angular distributions at higher ($E_p = 1.214$ MeV) and lower ($E_p =$ 1.263 MeV) energies are found to be in good agreement with the fit. No explanation for this discrepancy could be found.

A few of the data sets analyzed did not have an absolute cross-section scale determined. For these cases, the data sets were fit with a free normalization parameter for the cross section. Table XI of Appendix B lists the different data sets which had free cross-section normalizations along with the normalization factor that was multiplied by the original scale. Most of the normalizations are referenced to the scale of the figure where they were obtained. The exception to this is the ^{12}C(α, α_0)^{12}C angular distribution data from Ref. [24] which are referenced to the data which are available in the EXFOR [51] database.

The data from Refs. [35,36] have improved statistical measurements but suffer from large systematic uncertainties. For this reason, these data sets are normalized to the on-resonance measurements of Ref. [10]. The cross sections from Ref. [36] are multiplied by a normalization factor of 1.04, which was well within the 10% systematic uncertainty quoted in that work. The cross sections of Ref. [35] are multiplied by

a significantly larger factor of 1.23 but this value remains within the large systematic uncertainty estimated in that work.

For nearly all of the levels examined, the lowest possible intrinsic/angular momentum couplings, for a given particle channel, are found to be sufficient to reproduce the data. The one exception is the 1^+ level at $E_x = 13.66$ MeV. For this level there are two possibilities for the allowed contributions of the intrinsic channel spin (s) for the lowest possible angular momentum (l) in the proton particle channel, $(s, l) = (0, 1)$ and $(1, 1)$. The analysis found that the partial width of the $(0, 1)$ channel was zero to within the uncertainty of the data.

A. Parameter uncertainties and correlations

The uncertainty calculations are based on the methods described in Refs. [60–62] and are implemented in other R-matrix calculations (e.g., Refs. [63,64]). The uncertainties quoted in Tables VIII, IX, and X of Appendix A approximate a 1σ ($\sim$68.3%) confidence level for a multiple parameter fit. The covariance and correlation matrices for the fit parameters are calculated using the MINUIT2 routine MINOS [43,65].

The uncertainties on the fit parameters are *statistical* only. That is, they result from purely the uncertainties quoted for each experimental data point. Depending on the experimental data set, they may not include corrections for effects like beam energy resolution, energy loss through targets, and detector geometry. In several cases, often where there are not much experimental data available, the statistical uncertainties dominate. In others, where the data points are quoted with high precision and are numerous, the statistical uncertainties may be quite small. The two main sets of parameters whose uncertainties are likely significantly affected by systematics are the energies of the levels and the α widths of states below the proton separation energy. Systematic uncertainties are not currently included in the calculation because of the impractical computation time which is required. The uncertainties given in Tables VIII, IX, and X of Appendix A must only be regarded as lower limits. Overall, good systematic agreement is found among the different data sets. This agreement is usually on the order of 5%.

The correlation among parameters is also investigated. The correlation coefficients for two different fit parameters range between 0 and 1, with 0 signifying that two parameters are completely independent and 1 signifying that two parameters have identical meaning. The correlation matrix was found to be quite useful in eliminating redundant fit parameters and in understanding which fit parameters have the most effect on the low-energy extrapolation of the S factor as discussed below.

B. Isospin considerations

There have been several discussions about the isospin mixing of the two $J^\pi = 1^-$ states at $E_x = 12.45$ ($T = 0$) and 13.09 MeV ($T = 1$) (e.g., Refs. [6,9,19,66]). The isospin mixing can be expressed as the linear combination

$$\begin{aligned} |12.45\rangle &= \alpha\,|1^-, 0\rangle + \beta\,|1^-, 1\rangle, \\ |13.09\rangle &= \beta\,|1^-, 0\rangle - \alpha\,|1^-, 1\rangle, \end{aligned} \tag{2}$$

where $|1^-, 0\rangle$ and $|1^-, 1\rangle$ are the pure eigenstates of (J^π, T) and $\alpha^2 + \beta^2 = 1$. Using this notation, the mixing ratio can be expressed as

$$\frac{\alpha^2}{\beta^2} = \frac{\gamma^2_{\alpha_0}(12.45)}{\gamma^2_{\alpha_0}(13.09)} = \frac{\gamma^2_{\gamma_0}(13.09)}{\gamma^2_{\gamma_0}(12.45)}, \tag{3}$$

where γ_{α_0} is the reduced ground-state α-particle width and γ_{γ_0} is the reduced width of the ground-state γ-ray transition. From the current analysis, it is found that

$$\begin{aligned} \frac{\gamma^2_{\alpha_0}(12.45)}{\gamma^2_{\alpha_0}(13.09)} &= \left(\frac{0.150(2)}{0.072(2)}\right)^2 = 4.34(27), \\ \frac{\gamma^2_{\gamma_0}(13.09)}{\gamma^2_{\gamma_0}(12.45)} &= \left(\frac{0.294(7)}{0.130(6)}\right)^2 = 5.11(53), \end{aligned}$$

giving similar results.

The examination of the isospin of higher-energy levels was also critical in understanding of the background pole components needed to reproduce the ^{15}N$(p, \gamma_0)^{16}$O data. At energies below the 1^- level at $E_x = 13.09$ MeV, the goodness of the fit can be attributed to the strong constraints on the resonance parameters provided by the additional reaction-channel data and a complete description of the different reaction components. This is most pronounced for Γ_p and Γ_{γ_0} partial widths of the level at $E_x = 12.45$ MeV, where only the product is constrained when the ^{15}N$(p, \gamma_0)^{16}$O data is fit alone.

At higher energies, however, the fit tends to overestimate the experimental data unless a significant background pole contribution is included, suggesting that other components to the cross section become important at these energies. As discussed in Sec. V F, background poles with large α widths were required to reproduce the observed α-scattering cross sections. However, the ^{12}C$(\alpha, \gamma_0)^{16}$O data of Ref. [37] limits the size of the 1^- background pole γ width to a few eV. Seemingly in contrast, in Sec. IV, it is shown that, with a proton width of order a few MeV, a γ width of the order of hundreds of eV is required to improve the fit.

The solution to this apparent discrepancy can be found by examining the isospin, T, of higher-energy 1^- states in ^{16}O. For isolated $T = 1$ levels, α decays to the 0^+ ground state are forbidden. For $T = 0$ levels, $E1$ transitions to the ground state are forbidden. For this reason, it is expected that contributions from higher-energy 1^- levels will be much less significant for the reaction ^{12}C$(\alpha, \gamma_0)^{16}$O than for ^{15}N$(p, \gamma_0)^{16}$O. For the current analysis, this implies that the contributions from higher-energy 1^- levels cannot be adequately described by a single background pole. Instead, at least two background poles are required, a $T = 0$ and a $T = 1$ for the $J^\pi = 1^-$ group.

The need for two groups of background poles based on isospin is reflected in the higher-energy data from the literature [17]. For example, in the ^{15}N$(p, \gamma_0)^{16}$O data of Ref. [66], a broad resonance was observed at $E_x \sim 17$ MeV which is characterized as a $T = 1$, $J^\pi = 1^-$ level. The data of

Ref. [66] are used to estimate a rough constraint on the proton width and the γ_0 width of the broad level of 500 keV and 75 eV, respectively. Inclusion of this background level, with the experimentally constrained partial widths, significantly improves the agreement between the higher-energy data of Ref. [10] and the *R*-matrix calculation. However, the quality of the fit is still not as good as that discussed in Sec. IV, suggesting that other higher-energy $T = 1$, $J^\pi = 1^-$ levels may also be important. In order to simulate the contributions from these levels, a fit was performed allowing the γ_0 width to vary as a free parameter, which resulted in a significantly larger value of $\Gamma_{\gamma_0} \sim 500$ eV.

C. Extrapolation of ^{15}N$(p,\gamma)^{16}$O

Taking into account the data for all the experimentally measured ^{16}O reaction channels significantly increases the constraints on the partial widths for the ^{15}N$(p, \gamma_0)^{16}$O fit as illustrated in Fig. 48. The vertical dashed lines in the figure indicate the central energies of the two 1^- levels at $E_x = 12.45$ and 13.09 MeV which dominate the ^{15}N$(p, \gamma_0)^{16}$O cross section. All fit parameters, constrained by data, are allowed to vary as free parameters and a consistent fit is achieved. The fit parameters obtained for the two 1^- levels at $E_x = 12.45$ and 13.09 MeV are given in Table IV.

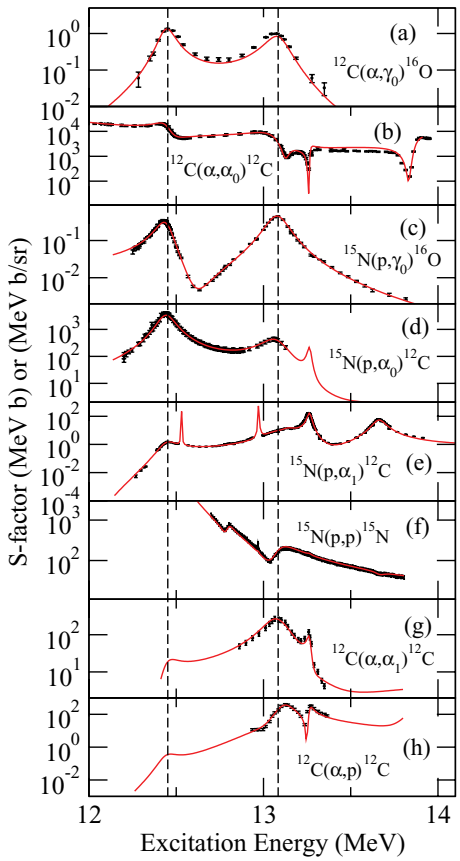

FIG. 48. (Color online) Comparison of the S factors for the different data sets and corresponding *R*-matrix calculations in the energy region above S_p. Part (a) shows the angle-integrated ^{12}C$(\alpha, \gamma_0)^{16}$O data of Ref. [26], (b) the ^{12}C$(\alpha, \alpha_0)^{12}$C data of Refs. [24,33,48] at $\theta_{\rm lab} \approx 165^\circ$, (c) the ^{15}N$(p, \gamma_0)^{16}$O data of Ref. [10], (d) the ^{15}N$(p, \alpha_0)^{12}$C data of Refs. [26,31], (e) the angle-integrated ^{15}N$(p, \alpha_1\gamma)^{12}$C data of Ref. [40], (f) the ^{15}N$(p, p)^{15}$N data of Ref. [19] at $\theta_{\rm lab} = 158.7^\circ$, (g) the ^{12}C$(\alpha, \alpha_1)^{12}$C data from Ref. [23] at $\theta_{\rm lab} = 90^\circ$, and (h) the ^{12}C$(\alpha, p)^{15}$N data of Ref. [23] at $\theta_{\rm lab} = 90^\circ$. The black dashed lines indicate the energies of the two 1^- levels at $E_x = 12.45$ and 13.09 MeV.

TABLE IV. Summary of the parameters for the two 1^- levels whose deexcitations dominate the ^{15}N$(p, \gamma_0)^{16}$O cross section. The $J^\pi = 1^-$, $T = 1$ background pole, labeled BGP, is also included where its ground-state γ width is allowed to vary as a free fit parameter.

J^π	E_x (MeV)	Channel	$(s, l/\Pi L)$	Γ_i (keV)	
				This work	Literature [17]
1^-	12.445	α_0	(0,1)	100(1)	102(4)
		α_1	(2,1)	0.030(2)	0.025
		p	(1,0)	1.45(3)	0.9(1)
		γ_0	$(0,E1)$	0.0067(3)	0.012(2)
1^-	13.09	α_0	(0,1)	28.5(6)	45(18)
		α_1	(2,1)	0.58(4)	1
		p	(1,0)	110(2)	100
		γ_0	$(0,E1)$	0.043(1)	0.032(5)
1^- (BGP)	17.09[a]	p	(1,0)	500[b]	
		γ_0	$(0,E1)$	0.5(1)	

[a]Fixed at the energy of the broad $T = 1$ state at $E_x = 17.09(4)$ [17].
[b]Fixed at 500 keV.

The main components of the fitting, resonance associated with the 1^- levels at $E_x = 12.45$ and 13.09 MeV, $E1$ external capture to the ground state, and a $T = 1$ $J^\pi = 1^-$ background pole, are shown in Fig. 49 extrapolated down to $E_{\rm c.m.} = 10$ keV. The energy dependence of the background pole and the external capture are nearly identical in the low-energy region. By including a false data point at $E_{\rm c.m.} = 10$ keV with

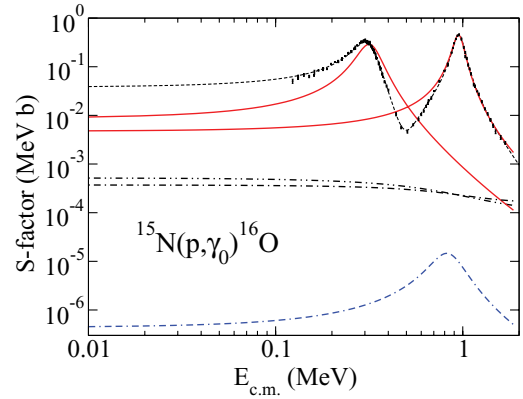

FIG. 49. (Color online) Comparison of the different reaction components included in the fitting of the ^{15}N$(p, \gamma_0)^{16}$O data. Only the ground-state data from Ref. [10] are shown for clarity. The full fit is shown by the dashed black line, the resonance components by the solid red line for the 1^- levels and dot-dash-dashed blue line for the 2^+ level, the ground-state external capture by the dot-dot-dashed black line, and the background pole by the dashed-dotted black line.

TABLE V. Values of $S(0)$ for ^{15}N$(p,\gamma_0)^{16}$O from previous works and the present work.

Ref.	$S(0)$ (keV b)
Hebbard [5]	32
Rolfs and Rodney [6]	64(6)
Barker [49] (RR)	≈50–55
Barker [49] (HH)	≈35
Mukhamedzhanov *et al.* [8]	36.0(60)
LeBanc *et al.* [10]	39.6(26)
Mukhamedzhanov *et al.* [9]	33.1–40.1
This work	40(3)

a free normalization parameter and calculating the correlation matrix (see Sec. VI A), a measure of the sensitivity of the S-factor extrapolation to the fit parameters is obtained. Since the proton ANC of the ground state is fixed, by far the most sensitive fit parameter is the ground-state γ partial width of the $T = 1$, $J^\pi = 1^-$ background pole, having a correlation coefficient of ∼0.7.

The value of $S(0)$ for the ground state is given in Table V and is compared to previous estimates from Refs. [5,6,8–10,49]. The uncertainty in $S(0)$ for the ground-state transition includes a 4% statistical uncertainty and a 5% systematic uncertainty as reported in Ref. [10].

The new measurement of the excitation curves of the three dominant cascade transitions allows for estimates of the contributions from these transitions. Similarly to the ground-state transition, the excitation curves from the cascade transitions were extrapolated to $E_{\text{c.m.}} = 10$ keV. The values of the low-energy S factors and their uncertainty estimates are given in Table VI compared to the ground state. The value of the $E_x = 6.049$ MeV transition is found to be negligible at the current level of uncertainty, but the contributions from the $E_x = 6.130$ and 7.117 MeV transitions approach the level of statistical uncertainty of the ground-state transition. The uncertainties of the low-energy S factors for the three cascade transitions remain large due to the significant statistical uncertainties of the data as well as a possibly incomplete description of the different cross-section components [40].

The total low-energy S-factor, ground-state-plus-cascade transitions for the reaction ^{15}N$(p,\gamma)^{16}$O is given in Table VI. The multiple-channel analysis gives a value for $S(0)$ of 41 keV b with a reduced χ^2 of 3.2 for ^{15}N$(p,\gamma_0)^{16}$O data of Ref. [10] compared to the value of ∼38 keV b obtained from the three fits in Sec. IV, which all had similar reduced χ^2 values of 1.7. The increase in χ^2 using the multiple-channel fit is the result of the constraints placed on the fit by the other reaction-channel data. The reduced χ^2 value of 1.7, found when only the ^{15}N$(p,\gamma_0)^{16}$O data are fit, is viewed as a misleadingly good fit considering several of the fit parameters resulted in unphysical values.

TABLE VI. Contributions to the total ^{15}N$(p,\gamma)^{16}$O S factor at $E_{\text{c.m.}} = 10$ keV. The quoted uncertainties are the sum of the statistical uncertainty deduced from the multiple parameter uncertainty analysis and a 5% systematic uncertainty as given in Ref. [10].

Transition	$S(0)$ (keV b)
Ground state	40(3)
6.049	0.04(2)
6.130	0.3(1)
7.117	0.9(3)
Total	41(3)

1. *Sensitivity of the proton ANC$_{gs}$ to the multichannel analysis*

Throughout the present analysis the proton ANC of the ground state of ^{16}O is fixed to the recommended value of 13.9 fm$^{-1/2}$ determined by Ref. [8] using the transfer reaction ^{15}N$(^3$He$, d)^{16}$O. To test the level of constraint on the proton ANC of the ground state by the multiple-channel analysis, a fit was performed where the proton ANC of the ground state was allowed to vary as a free parameter in addition to the other normal fit parameters. The fit resulted in a value for the proton ANC of the ground state of 28(17) fm$^{-1/2}$ which is consistent with, but less precise than, the transfer reaction value of 13.9(19) fm$^{-1/2}$. This confirms that, even in the multiple-channel approach, the ^{15}N$(p,\gamma)^{16}$O cross-section data offers rather limited constraint on the value of the proton ANC of the ground state.

Despite the much larger value of the proton ANC of the ground state, the extrapolated value of $S(0)$ for the ground-state transition is still found to be 40(3) keV b. This is because the larger contribution of the external capture is offset by a smaller contribution from the background pole. Since the energy dependence of the two cross-section components, external capture and background pole, are so similar over the energy range of the data (see Fig. 49), a similar fit can always be achieved over a wide range of ANC values given an adjustable background pole contribution. Therefore, only the sum of the two contribution can be constrained. The ambiguity between the background pole and external capture cross-section components is a result of the relative strength of these components compared to the broad resonance components. What is somewhat unique to the case of the ^{15}N$(p,\gamma)^{16}$O reaction is that there is no energy region where the cross section is dominated by external capture. As shown in Ref. [6], the interference between the resonances and the capture component of the cross section is critical in reproducing the experimental data in the region between the two resonances, but the direct component itself remains only a small fraction of the total cross section. This is similar to the situation which occurs at low energies: The tails of the resonances still dominate the cross section but the interference term between the resonances and the external capture again becomes quite significant. While this result is somewhat disappointing from the view of determining nuclear structure information of ^{16}O because it means that the cross-section data cannot be used to well constrain the ANC, it is quite convenient for the determination of the low-energy cross section of the ^{15}N$(p,\gamma)^{16}$O, which is the desired quantity for nuclear astrophysics.

2. *Other possible cross-section contributions*

With the additional constraints from other reaction channels placed on the partial widths of the ^{15}N$(p,\gamma_0)^{16}$O data, a number of other possible contributions to the ^{15}N$(p,\gamma_0)^{16}$O cross section could be tested. Capture strengths to several other states in addition to the ground state are reported in Ref. [8]. These contributions were tested throughout the fitting and were verified to have no significant effect. Narrow resonances which were previously neglected were also introduced with their parameters fixed, their inclusion had no significant effect. Another natural parity resonance has a ground-state γ transition in this energy region, this is the 2^+ resonance at $E_x = 12.95$ MeV. Inclusion of this γ transition was necessary to reproduce the angular distributions for ^{12}C$(\alpha,\gamma_0)^{16}$O data over the same excitation energy range and was therefore constrained by that data. The contribution to the ^{15}N$(p,\gamma_0)^{16}$O cross section for this resonance is shown in Fig. 49 and is verified to be too weak to have a significant effect. The 1^+ level at $E_x = 13.66$ MeV could decay by $M1$ de-excitation to the ground state but no evidence for this is observed (contrary to Ref. [6]). It is also possible that $E3$ deexcitation to the ground state could occur from the two 3^- levels at $E_x = 13.13$ and 13.27 MeV but, because of the high multipolarity, it is expected that these will also have no significant contribution.

D. Extrapolation of ^{15}N$(p,\alpha)^{12}$C

The current global analysis allows for several additional constraints on the R-matrix fit of the ^{15}N$(p,\alpha_0)^{12}$C data which have not been fully considered in past analyses. These include the fitting of multiple channels simultaneously, the consideration of angular distribution data, and the more complete description of the level structure. Rather conveniently, the same two 1^- levels which dominate the ^{15}N$(p,\gamma_0)^{16}$O cross section also dominate this reaction channel (see Fig. 48), making the multichannel analysis quite useful. One difference in this reaction channel is that the broad 2^+ level at $E_x = 12.97$ MeV contributes enough to make it critical in reproducing the angular distribution data as demonstrated in Ref. [29] and shown in Fig. 50.

The R-matrix technique has been used recently by Refs. [49,50] to estimate the low-energy S factor using the data of Refs. [30,31,34], which are all available in tabulated form. In these analyses, a two-level R-matrix approach has been used which considers the 1^- levels at $E_x = 12.45$ and 13.09 MeV. The current analysis examines the more complete level structure by also including the contributions from the 2^+ level at $E_x = 12.96$ MeV and the 3^- levels at $E_x = 13.14$ and 13.27 MeV. Additional data considered in this reaction channel include the angular distributions of Refs. [29,31], the higher-energy differential cross-section measurements of Refs. [18,20,21], and the yield-ratio data of Ref. [38].

In general, the global fit is in good agreement with the experimental data, but one key area of disagreement is the lowest-energy data region ($E_p < 0.17$ MeV) of Ref. [31], where the R-matrix fit always overestimates the data points. This is in contrast to the low-energy data of Ref. [30], where excellent agreement is found over the entire region of the data. This same issue has also been encountered by Ref. [49], who

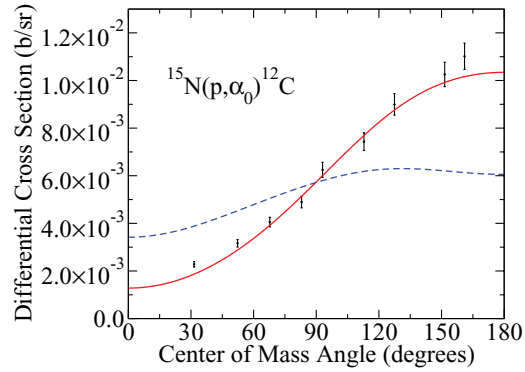

FIG. 50. (Color online) An example ^{15}N$(p,\alpha_0)^{12}$C angular distribution measurement at $E_p = 0.75$ MeV from Ref. [31]. The solid red line represents the current R-matrix fit to the data including the two 1^- levels at $E_x = 12.45$ and 13.09 MeV and the 2^+ level at $E_x = 12.97$ MeV. In contrast, the dashed blue line represents the angular distribution which would result if only the two 1^- levels were included in the calculation.

likewise found good agreement with the low-energy data of Ref. [30] but not those of Ref. [31]. In contrast, Ref. [50] reports R-matrix fits which are in good agreement with the low-energy data of Refs. [30,31,34] but seems to achieve this by not placing the same tight constraints on the partial widths of the higher-energy 1^- level at $E_x = 13.09$ MeV.

The Trojan horse data of Ref. [34] are also considered here but the data set is truncated above $E_p = 0.32$ MeV where the data suffer from experimental resolution effects [50]. Since the data lack an independent normalization they have been allowed to vary freely during the fitting. This results in a 6% increase in the cross-section values reported in Ref. [34]. The current fit then falls with in the uncertainties of all of the Trojan horse data except for the lowest-energy data point at $E_{\text{c.m.}} = 19.2$ keV.

An extrapolation of the global fit for the ^{15}N$(p,\alpha_0)^{12}$C S factor, which includes the data from both Refs. [31] and [30], leads to a value of $S(0) = 95(6)$ MeV b and is shown in Fig. 51. This larger value of the low-energy S factor results mainly from the increased constraints on the partial widths of the higher-energy $E_x = 13.09$ MeV level and the consideration of the angular distribution data. If only the excitation curve data were considered, one could, in principle, add a 1^- background pole contribution which would interfere with the lowest-energy level at $E_x = 12.45$ MeV and decrease the low-energy cross section. However, the addition of such a background component would cause significant disagreement in the higher-energy data region. Based on these further limitations, it is not possible to produce the required level of destructive interference in the low-energy region which would match the data of Ref. [31]. Even if the data of Ref. [30] are removed from the analysis the fit results in $S(0) \approx 92$ MeV b. Table VII summarizes the resulting $S(0)$ values from the present and previous works.

One possible solution to the disagreement between the data of Ref. [31] and the global fit is an underestimation in energy calibration uncertainty. At these low energies, the S-factor extrapolation is extremely sensitive to the energy of the data

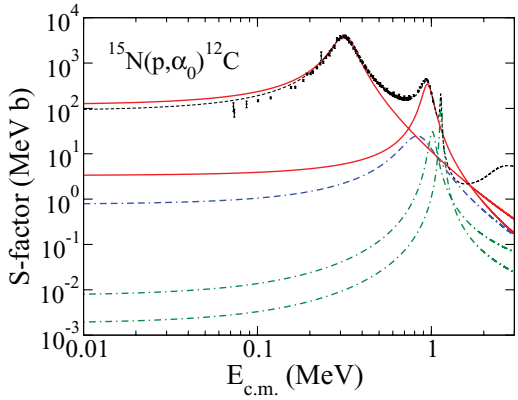

FIG. 51. (Color online) Comparison of the different reaction components included in the fitting of the ^{15}N$(p,\alpha_0)^{12}$C data. Only data from Refs. [26,31] are shown for clarity. The full fit is shown by the dashed black line, the resonance components by the solid red for the 1^- levels, dot-dash-dashed blue line for the 2^+ levels, and dot-dashed green line for the 3^- levels.

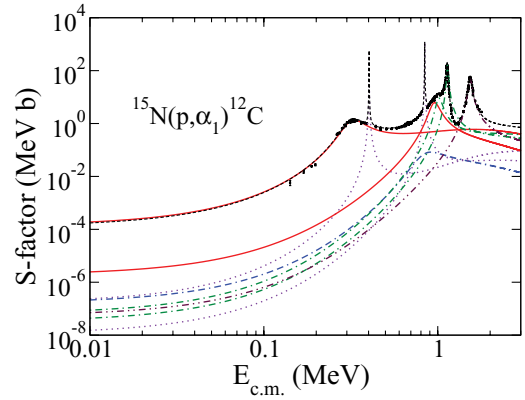

FIG. 52. (Color online) Comparison of the different reaction components included in the fitting of the ^{15}N$(p,\alpha_1)^{12}$C data. The data are from Ref. [40]. The full fit is shown by the dashed black line, the resonance components by solid red lines for the 1^- levels, the dot-dot-dashed maroon line for the 1^+ level, the dot-dash-dashed blue line for the 2^+ level, the dotted violet lines for the 2^- levels, and the dot-dashed green lines for the 3^- levels.

points. The data of Ref. [31] report an uncertainty in energy of 0.5 keV at $E_p < 0.36$ MeV (i.e., the gas target data) but this may be somewhat underestimated since the recommended energy of the ^{18}O$(p,\alpha)^{15}$N resonance used to cross-check the energy calibration has changed from the value of $E_p =$ 152(1) keV [67] used by Ref. [31] to 150.94(5) keV [68]. If the energies of this data from Ref. [31] are adjusted down in energy by 1 keV, they come into better agreement with the current analysis. If they were adjusted down by 3 keV, they would be in excellent agreement, matching the energy dependence over the entire range. However, such a large shift in energy is difficult to explain considering the given uncertainty.

Another solution may be the presence of an additional reaction component to the cross section which is not properly modeled by the current framework. This would most likely be a direct contribution as discussed in Ref. [31] and described in Ref. [69], for example.

The recent ^{15}N$(p,\alpha_1\gamma)^{12}$C data of Ref. [40] have been extrapolated to low energy and a value of $S(0) = 0.164(13)$ keV b is found which is consistent with the estimate given in Ref. [6] of ≈0.1 keV b. The analysis confirms that this reaction

TABLE VII. Values of $S(0)$ for ^{15}N$(p,\alpha_0)^{12}$C from previous works and the present work.

Ref.	$S(0)$ (MeV b)
Schardt *et al.* [18]	≈64[a]
Zyskind and Parker [30]	78(13)
Redder *et al.* [31]	65(4)
La Cognata *et al.* [34]	68(11)[b]
Barker [49]	≈80[c]
La Cognata *et al.* [50]	73(5)
this work	95(6)

[a]Given at $E_{c.m.} = 30$ keV.
[b]Trojan horse data normalized to Ref. [31].
[c]Analysis based on the data of Refs. [18,31,34]. Reference [50] data are reanalyzed and give 82(10) MeV b.

TABLE VIII. Excitation energies for the levels considered in this work compared to those from the literature. Particle bound and narrow level energies are fixed to values from the literature. Background pole energies are also fixed.

Res no.	J^π	E_x (MeV)	
		This work	Ref. [17]
1	0^-	12.796(2)	12.796(4)
2[a]	0^+	Fixed	0
3	0^+	Fixed	6.0494(10)
4[b]	0^+	15	
5	1^-	Fixed	7.11685(14)
6	1^-	9.591(2)	9.585(11)
7	1^-	12.445	12.440(2)
8	1^-	13.090	13.090(8)
9[b]	1^-	Fixed	17.090(40)
10[b]	1^-	20	
11	1^+	13.665(3)	13.664(3)
12	2^-	Fixed	12.530(1)
13	2^-	Fixed	12.9686(4)
14	2^+	Fixed	6.9171(6)
15	2^+	11.5089(3)	11.520(4)
16	2^+	12.967(2)	13.02(1)
17[b]	2^+	15	
18	3^-	Fixed	6.12989(4)
19	3^-	11.505(2)	11.600(20)
20	3^-	13.142(1)	13.129(10)
21	3^-	13.265	13.259(2)
22[b]	3^-	20	
23	4^+	10.3608(2)	10.356(3)
24	4^+	13.850(3)	13.869(2)
25[b]	4^+	15	
26[b]	5^-	Fixed	14.660(20)

[a]Ground state.
[b]Background pole.

channel has no significant effect on the ^{15}N$(p,\alpha)^{12}$C reaction rate at stellar energies. The extrapolation is shown in Fig. 52.

VII. CONCLUSION

It has been demonstrated that a multiple-entrance-/exit-channel *R*-matrix approach provides significant improvement in the analysis of resonance and direct capture reaction channels associated with ^{16}O compound nucleus. The technique is especially valuable when multiple entrance channels are possible and experimental data exist for the various reaction channels. Using this method, a consistent fit was obtained for all available reaction channels demonstrating the level of agreement between the wide variety of experimental data. An examination of the correlation coefficients of the fit parameters shows clearly that the uncertainty of the background pole contribution has the largest effect on the uncertainty in the extrapolated ^{15}N$(p,\gamma)^{16}$O S factor to low energy when a constant proton ANC of the ground state is assumed. Further, it is found that a wide range of values for the proton ANC of the ground state, which include the precise value measured using a transfer reaction, combined with a background pole contribution, always produces the same extrapolated value of the total S factor at low energy, 41(3) keV b, given the very similar energy dependence of the two reaction components. For the reaction ^{15}N$(p,\alpha)^{12}$C, examination of the angular distribution and higher-energy data has led to a larger value for the low-energy S factor of 95(6) MeV b. As the main objective of this analysis, a better constrained, consistent, and physically justifiable fit of the ^{15}N$(p,\gamma_0)^{16}$O and ^{15}N$(p,\alpha_0)^{12}$C cross sections has been achieved, leading to a more reliable extrapolation of the S factors to stellar energies.

ACKNOWLEDGMENTS

The authors are indebted to R. E. Azuma for his contributions, numerous discussions, and critical remarks on both this work and the *R*-matrix code. R.J.D. would also like to thank A. Villano for many useful discussions concerning multiple parameter fitting. This work was funded by the National Science Foundation through Grant No. Phys-0758100 and the Joint Institute for Nuclear Astrophysics through Grant No. Phys-0822648.

APPENDIX A: *R*-MATRIX FIT PARAMETERS

Tables VIII, IX, and X give the *R*-matrix parameters which characterize the cross section in the figures shown though out

TABLE IX. Particle partial widths for the levels considered in this work compared with those from the literature. Widths for narrow levels are fixed to the values from the literature. ANCs are fixed to values determined from transfer reactions when available. α-particle ANCs for the bound states at $E_x = 6.049$ and 6.130 MeV are fixed at values determined from the cascade data of Ref. [37].

Res. no.	(s,l)	Γ_{α_0} (keV)/ANC (fm$^{-1/2}$)		(s,l)	Γ_p (keV)/ANC (fm$^{-1/2}$)		(s,l)	Γ_{α_1} (keV)	
		This work	Ref. [17,70]		This work	Ref. [8,17]		This work	Ref. [17]
1				(0,0)	52(3)	40			
2				(1,1)	Fixed	13.9(19)			
3	(0,0)	−1800							
4	(0,0)	−12 300(300)		(1,1)	400(100)				
5	(0,1)	Fixed	$2.0(4) \times 10^{14}$	(1,0)	Fixed	0.98(12)			
6	(0,1)	393(2)	420(20)						
7	(0,1)	100(1)	102(4)	(1,0)	1.45(3)	0.9(1)	(2,1)	−0.030(2)	0.025
8	(0,1)	−28.5(6)	45(18)	(1,0)	110(2)	100	(2,1)	0.58(4)	1
9				(1,0)	500	380(40)			
10	(0,1)	16 800(400)							
11				(1,1)	−8.1(7)	10	(2,2)	64(6)	59(6)
12				(0,2)	Fixed	0.016(3)	(2,1)	Fixed	0.092(10)
13				(0,2)	Fixed	1.04(7)	(2,1)	Fixed	0.30(6)
14	(0,2)	Fixed	$1.14(20) \times 10^5$	(1,1)	Fixed	0.45(13)			
15	(0,2)	84.4(5)	71(5)						
16	(0,2)	−349(3)	150(10)	(1,1)	1.5(2)		(2,0)	−0.5(2)	
17	(0,2)	5780(30)		(1,1)	−5(3)				
18	(0,3)	150		(1,2)	Fixed	1.88(23)			
19	(0,3)	889(4)	800(100)						
20	(0,3)	73(1)	90(14)	(1,2)	−0.97(5)	1	(2,1)	20.9(6)	20
21	(0,3)	11.0(3)	9(4)	(1,2)	3.5(1)	4.1	(2,1)	10.3(4)	8.2(11)
22	(0,3)	−22 100(400)							
23	(0,4)	26.1(2)	26(3)						
24	(0,4)	78(7)	49				(2,2)	39(5)	23
25	(0,4)	2380(50)							
26	(0,5)	1300(20)	670(15)	(1,4)	8				

TABLE X. Radiation widths for the γ-ray transitions considered in this work compared with those from the literature. Internal and external radiative reduced width amplitudes are also provided. Cascade transition γ-ray widths for the 2^+ and 3^- levels at $E_x = 11.51$ MeV are fixed at values determined from the cascade data of Ref. [37].

Res. no.	E_f (MeV)	$(s, \Pi L)$	$\gamma_{\gamma(\text{int})}$ (MeV$^{-1/2}$)	$\gamma_{\gamma(\text{ext})}$ (MeV$^{-1/2}$)	Γ_γ (eV)	
					This work	Ref. [17]
1	7.117	(1,$M1$)	0.28		2.7(2)	2.5(2)
5	0	(0,$E1$)	0.018	0.006	Fixed	0.055(3)
	6.049	(0,$E1$)	0.001		Fixed	$<0.3 \times 10^{-6}$
	6.130	(3,$E2$)	0.30	0.19	Fixed	$46(10) \times 10^{-6}$
	6.917	(2,$E1$)	0.021	0.002	Fixed	$<1 \times 10^{-6}$
6	0	(0,$E1$)	−0.011		−0.0168(4)	0.0156
	6.917	(2,$E1$)	0.012		0.00042(3)	0.0014
	7.117	(1,$E2$)	2.0	$1.2 + i0.5$	0.0043(9)	0.0078
7	0	(0,$E1$)	0.072	0.058	6.7(3)	12(2)
	6.049	(0,$E1$)	−0.041		−0.09(4)	0.12(6)
	6.130	(3,$E2$)	−1.51	$0.37 + i0.11$	−0.07(3)	
	7.117	(1,$M1$)	0.064		0.13(5)	
8	0	(0,$E1$)	0.23	0.06	43(1)	32(5)
	6.049	(0,$E1$)	0.056		Fixed	0.24(5)
	6.130	(3,$E2$)	−2.2	0.2	−0.4(2)	
	7.117	(1,$M1$)	0.17		Fixed	1.35(40)
9	0	(0,$E1$)	0.60	$0.04 + i0.02$	500(100)	75
12	0	(0,$M2$)	0.13		Fixed	0.033(5)
	6.130	(3,$M1$)	0.017		Fixed	2.1(2)
	7.117	(1,$M1$)	0.010		Fixed	0.5(1)
13	0	(0,$M2$)	0.12		Fixed	0.034(9)
	6.130	(3,$M1$)	0.016		Fixed	2.3(2)
	7.117	(1,$M1$)	0.0064		Fixed	0.44(10)
14	0	(0,$E2$)	0.98	0.01	Fixed	0.097(3)
	6.049	(0,$E2$)	0.84	−0.47	Fixed	$27(3) \times 10^{-6}$
	6.130	(3,$E1$)	0.0020	0.0061	Fixed	$\leqslant 9 \times 10^{-6}$
15	0	(0,$E2$)	0.68		Fixed	0.61(2)
	6.049	(0,$E2$)	−0.82	$-0.27 - i0.20$	0.04	
	6.130	(3,$E1$)	−0.022		0.02	
	6.917	(2,$E2$)	0.90	$0.26 + i0.20$	0.02	
	7.117	(1,$E1$)	0.015		0.005	
16	0	(0,$E2$)	−0.61	0.03	Fixed	0.7(2)
18		(0,$E3$)	0.37		Fixed	$26(13) \times 10^{-6}$
19	6.130	(3,$E2$)	0.06	$0.58 + i0.24$	0.01	
	6.917	(2,$E1$)	0.024		0.01	
	7.117	(1,$E2$)	0.99	$0.81 + i0.50$	0.03	
20	0	(0,$E3$)	1.1		Fixed	>0.010
	6.130	(3,$M1$)	−0.35		8	
21	6.130	(3,$M1$)	0.24		5(3)	9.2(15)[a]
23	6.917	(2,$E2$)	3.3	$0.7 + i0.1$	0.046(1)	0.062(6)

[a]Ref. [71]

this work. Several parameters which were not constrained well by the data have been fixed in the analysis. The sensitivity of the fixed parameters have been tested against the extrapolation of the low-energy S factor of the ^{15}N$(p,\gamma)^{16}$O reaction and reasonable variations are found to have no significant effect. It should be noted that the quoted uncertainties are statistical only. That is, they are determined from only the statistical uncertainties of the data points.

APPENDIX B: DATA SET NORMALIZATIONS

Several data sets, mostly angular distribution measurements in older works, report only relative yield measurements. The shape of the yield curves can still provide significant constraints on the R-matrix fit. To include these data, they are scaled to the R-matrix calculation. The scaling factors are presented in Table XI along with the reference and figure from

TABLE XI. Scaling factors for data sets which have no reported absolute scale. The factors represent the multiplicative scaling used between the figure from which the data were digitized and the cross section deduced by use of the *R*-matrix calculation. The exceptions are the angular distribution data from Ref. [24] where the data are scaled to those previously digitized by Ref. [51].

Figure no. (this work)	Ref./Source	Normalization
11(a)	[31]/Fig. 5	2.5×10^{-6}
11(b)	[31]/Fig. 5	2.9×10^{-4}
11(c)	[31]/Fig. 5	7.1×10^{-3}
11(d)	[31]/Fig. 5	5.0×10^{-3}
11(e)	[31]/Fig. 5	4.3×10^{-3}
11(f)	[31]/Fig. 5	6.3×10^{-3}
22(a)	[52]/Fig. 2	5.2×10^{-3}
22(b)	[52]/Fig. 2	2.7×10^{-3}
22(c)	[52]/Fig. 2	1.6×10^{-3}
22(d)	[52]/Fig. 2	1.1×10^{-3}
23(a)	[52]/Fig. 2	2.1×10^{-2}
23(b)	[52]/Fig. 2	7.1×10^{-3}
23(c)	[52]/Fig. 2	8.4×10^{-4}
35(a)	[24]/Fig. 5 (EXFOR)	1.06
35(b)	[24]/Fig. 5 (EXFOR)	1.13
35(c)	[24]/Fig. 5 (EXFOR)	1.08
35(d)	[24]/Fig. 5 (EXFOR)	1.01
35(e)	[24]/Fig. 5 (EXFOR)	0.96
35(f)	[24]/Fig. 5 (EXFOR)	1.06
36(a)	[24]/Fig. 5 (EXFOR)	0.95
36(b)	[24]/Fig. 5 (EXFOR)	0.87
36(c)	[24]/Fig. 5 (EXFOR)	0.83
36(d)	[24]/Fig. 5 (EXFOR)	0.82
36(e)	[24]/Fig. 5 (EXFOR)	1.02
Not shown	[24]/Fig. 5 (EXFOR)	0.97
36(f)	[24]/Fig. 5 (EXFOR)	0.91
37(a)	[24]/Fig. 5 (EXFOR)	0.86
37(b)	[24]/Fig. 5 (EXFOR)	0.78
37(c)	[24]/Fig. 5 (EXFOR)	0.96
37(d)	[24]/Fig. 5 (EXFOR)	0.73
37(e)	[24]/Fig. 5 (EXFOR)	1.21
37(f)	[24]/Fig. 5 (EXFOR)	1.31
38(a)	[24]/Fig. 5 (EXFOR)	1.54
38(b)	[24]/Fig. 5 (EXFOR)	1.00
38(c)	[24]/Fig. 5 (EXFOR)	0.86
38(d)	[24]/Fig. 5 (EXFOR)	1.01
39	[33]/Table I	1.46
46(a)	[22]/Fig. 3	3.1×10^{-9}
46(b)	[25]/Fig. 6	2.3×10^{-9}
46(c)	[25]/Fig. 6	2.2×10^{-9}
46(c)	[28]/Table V	2.00(fixed)
46(d)	[22]/Fig. 3	2.1×10^{-9}
46(d)	[25]/Fig. 6	1.7×10^{-9}
47(a)	[22]/Fig. 4	2.5×10^{-9}
47(b)	[22]/Fig. 4	3.6×10^{-9}
47(c)	[25]/Fig. 7	2.3×10^{-9}
47(d)	[22]/Fig. 4	2.7×10^{-9}
47(d)	[25]/Fig. 7	2.0×10^{-9}
47(e)	[22]/Fig. 4	2.2×10^{-9}
47(f)	[25]/Fig. 7	1.6×10^{-9}

which the data were taken as well as the figure in which the data are presented in this work.

APPENDIX C: ADDITIONAL ^{15}N(p, γ_0)^{16}O DATA

Additional data from Ref. [10] have been recovered. These data were not previously published because significant target thickness corrections were necessary in order to extract the cross sections. These corrections have been recently implemented resulting in the new data given in Table XII.

TABLE XII. Additional ^{15}N(p, γ_0)^{16}O data from Ref. [10]. In addition to the statistical uncertainties the data have an over all systematic uncertainty of 5% as described in Ref. [10].

E_p (MeV)	Cross section (b)	Uncertainty (b)
0.1315	2.17×10^{-9}	2.1×10^{-10}
0.1407	4.62×10^{-9}	4.5×10^{-10}
0.1408	4.65×10^{-9}	3.9×10^{-10}
0.1511	9.14×10^{-9}	5.6×10^{-10}
0.1612	1.40×10^{-8}	7.7×10^{-10}
0.1711	2.32×10^{-8}	9.8×10^{-10}
0.1807	4.35×10^{-8}	1.3×10^{-9}
0.1912	6.77×10^{-8}	3.4×10^{-9}
0.1913	7.08×10^{-8}	3.3×10^{-9}
0.2009	9.73×10^{-8}	2.9×10^{-9}
0.2112	1.71×10^{-7}	5.4×10^{-9}
0.2211	2.52×10^{-7}	5.1×10^{-9}
0.2306	3.31×10^{-7}	1.1×10^{-8}
0.2407	4.82×10^{-7}	1.7×10^{-8}
0.2509	7.31×10^{-7}	1.6×10^{-8}
0.2608	1.06×10^{-6}	2.2×10^{-8}
0.2707	1.42×10^{-6}	3.3×10^{-8}
0.2806	1.97×10^{-6}	6.6×10^{-8}
0.2906	2.78×10^{-6}	6.7×10^{-8}
0.3007	3.74×10^{-6}	5.9×10^{-8}
0.3105	4.76×10^{-6}	6.6×10^{-8}
0.3201	5.67×10^{-6}	6.2×10^{-8}
0.3301	6.50×10^{-6}	8.2×10^{-8}
0.3400	6.57×10^{-6}	6.3×10^{-8}
0.3499	6.38×10^{-6}	8.4×10^{-8}
0.3551	6.16×10^{-6}	1.1×10^{-7}
0.3599	5.82×10^{-6}	8.2×10^{-8}
0.3648	5.75×10^{-6}	2.0×10^{-7}
0.3698	5.09×10^{-6}	7.9×10^{-8}
0.3795	4.31×10^{-6}	9.1×10^{-8}
0.3845	4.07×10^{-6}	1.5×10^{-7}
0.3894	3.98×10^{-6}	9.3×10^{-8}
0.3944	3.26×10^{-6}	1.1×10^{-7}
0.3995	2.99×10^{-6}	6.3×10^{-8}

[1] G. R. Caughlan and W. A. Fowler, Astrophys. J. **139**, 1180 (1964).
[2] W. A. Fowler, Rev. Mod. Phys. **56**, 149 (1984).
[3] G. Imbriani, M. Limongi, L. Gialanella, F. Terrasi, O. Straniero, and A. Chieffi, Astrophys. J. **558**, 903 (2001).
[4] A. Wapstra, G. Audi, and C. Thibault, Nucl. Phys. A **729**, 129 (2003).
[5] D. Hebbard, Nucl. Phys. **15**, 289 (1960).
[6] C. Rolfs and W. S. Rodney, Nucl. Phys. A **235**, 450 (1974).
[7] F. C. Barker, Phys. Rev. C **78**, 044612 (2008).
[8] A. M. Mukhamedzhanov, P. Bém, V. Burjan, C. A. Gagliardi, V. Z. Goldberg, Z. Hons, M. La Cognata, V. Kroha, J. Mrázek, J. Novák *et al.*, Phys. Rev. C **78**, 015804 (2008).
[9] A. M. Mukhamedzhanov, M. La Cognata, and V. Kroha, Phys. Rev. C **83**, 044604 (2011).
[10] P. J. LeBlanc, G. Imbriani, J. Görres, M. Junker, R. Azuma, M. Beard, D. Bemmerer, A. Best, C. Broggini, A. Caciolli *et al.*, Phys. Rev. C **82**, 055804 (2010).
[11] L. L. Ames, Phys. Rev. C **25**, 729 (1982).
[12] N. I. Ashwood, M. Freer, N. L. Achouri, T. R. Bloxham, W. N. Catford, N. Curtis, P. J. Haigh, C. W. Harlin, N. P. Patterson, D. L. Price *et al.*, J. Phys. G: Nucl. Part. Phys. **36**, 055105 (2009).
[13] S. E. Darden, S. Sen, G. Murillo, M. Fernandez, J. Ramiez, A. Galindo, P. L. Jolivette, and B. P. Hichwa, Nucl. Phys. A **429**, 218 (1984).
[14] T. R. Ophel, P. Martin, S. D. Cloud, and J. M. Morris, Nucl. Phys. A **173**, 609 (1971).
[15] P. Tischhauser, A. Couture, R. Detwiler, J. Görres, C. Ugalde, E. Stech, M. Wiescher, M. Heil, F. Käppeler, R. E. Azuma *et al.*, Phys. Rev. C **79**, 055803 (2009).
[16] D. Schürmann, A. D. Leva, L. Gialanella, D. Rogalla, F. Strieder, N. D. Cesare, A. D'Onofrio, G. Imbriani, R. Kunz, C. Lubritto *et al.*, Eur. Phys. J. A **26**, 301 (2005).
[17] D. R. Tilley, H. R. Weller, and C. M. Cheves, Nucl. Phys. A **564**, 1 (1993).
[18] A. Schardt, W. A. Fowler, and C. C. Lauritsen, Phys. Rev. **86**, 527 (1952).
[19] F. B. Hagedorn, Phys. Rev. **108**, 735 (1957).
[20] F. B. Hagedorn and J. B. Marion, Phys. Rev. **108**, 1015 (1957).
[21] S. Bashkin, R. R. Carlson, and R. A. Douglas, Phys. Rev. **114**, 1543 (1959).
[22] J. D. Larson and R. H. Spear, Nucl. Phys. **56**, 497 (1964).
[23] I. V. Mitchell and T. R. Ophel, Nucl. Phys. **66**, 553 (1965).
[24] J. M. Morris, G. W. Kerr, and T. R. Ophel, Nucl. Phys. A **112**, 97 (1968).
[25] G. Kernel, W. M. Mason, and U. V. Wimmersperg, Nucl. Phys. A **167**, 352 (1971).
[26] F. Brochard, P. Chevallier, D. Disdier, V. Rauch, and F. Scheibling, J. Phys. France **34**, 363 (1973).
[27] M. D. Bruno, I. Massa, A. Uguzzoni, G. Bannini, E. Verondini, and A. Vitale, Il Nuovo Cimento A **27**, 1 (1975).
[28] T. R. Ophel, A. D. Frawley, P. B. Treacy, and K. H. Bray, Nucl. Phys. A **273**, 397 (1976).
[29] K. H. Bray, A. D. Frawley, T. R. Ophel, and F. C. Barker, Nucl. Phys. A **288**, 334 (1977).
[30] J. L. Zyskind and P. D. Parker, Nucl. Phys. A **320**, 404 (1979).
[31] A. Redder, H. W. Becker, H. Lorenz-Wirzba, C. Rolfs, P. Schmalbrock, and H. P. Trautvetter, Z. Physik A At. Nucl. **305**, 325 (1982).
[32] J. Sawicki, J. Davies, and T. Jackman, Nucl. Instrum. Methods B **15**, 530 (1986).
[33] Y. Feng, Z. Zhou, Y. Zhou, and G. Zhao, Nucl. Instrum. Methods B **86**, 225 (1994).
[34] M. La Cognata, S. Romano, C. Spitaleri, S. Cherubini, V. Crucillà, M. Gulino, L. Lamia, R. G. Pizzone, A. Tumino, R. Tribble *et al.*, Phys. Rev. C **76**, 065804 (2007).
[35] D. Bemmerer, A. Caciolli, R. Bonetti, C. Broggini, F. Confortola, P. Corvisiero, H. Costantini, Z. Elekes, A. Formicola, Z. Fülöp *et al.*, J. Phys. G: Nucl. Part. Phys. **36**, 045202 (2009).
[36] A. Caciolli, C. Mazzocchi, V. Capogrosso, D. Bemmerer, C. Broggini, P. Corvisiero, H. Costantini, Z. Elekes, A. Formicola, Zs. Fülöp *et al.*, Astron. Astrophys. **533**, A66 (2011).
[37] D. Schürmann, A. D. Leva, L. Gialanella, R. Kunz, F. Strieder, N. D. Cesare, M. D. Cesare, A. D'Onofrio, K. Fortak, G. Imbriani *et al.*, Phys. Lett. B **703**, 557 (2011).
[38] R. J. deBoer, P. J. LeBlanc, S. Falahat, G. Imbriani, J. Görres, S. O'Brien, E. Uberseder, and M. Wiescher, Phys. Rev. C **85**, 038801 (2012).
[39] R. J. deBoer, A. Couture, R. Detwiler, J. Görres, P. Tischhauser, E. Uberseder, C. Ugalde, E. Stech, M. Wiescher, and R. E. Azuma, Phys. Rev. C **85**, 045804 (2012).
[40] G. Imbriani, R. J. deBoer, A. Best, M. Couder, G. Gervino, J. Görres, P. J. LeBlanc, H. Leiste, A. Lemut, E. Stech *et al.*, Phys. Rev. C **85**, 065810 (2012).
[41] R. E. Azuma, E. Uberseder, E. C. Simpson, C. R. Brune, H. Costantini, R. J. de Boer, J. Görres, M. Heil, P. J. LeBlanc, C. Ugalde *et al.*, Phys. Rev. C **81**, 045805 (2010).
[42] E. Uberseder, R. deBoer, P. LeBlanc, E. Simpson, and R. Azuma, *AZURE User Manual* (2010), azure.nd.edu.
[43] F. James and M. Winkler, *Minuit User's Guide* (2008), http://www.cern.ch/minuit
[44] F. Barker and T. Kajino, Aust. J. Phys. C **44**, 369 (1991), http://www.publish.csiro.au/paper/PH910369.
[45] C. Angulo and P. Descouvemont, Nucl. Phys. A **690**, 755 (2001).
[46] C. R. Brune, Phys. Rev. C **66**, 044611 (2002).
[47] P. Descouvemont, *R*-matrix code (private communication).
[48] P. Tischhauser, R. E. Azuma, L. Buchmann, R. Detwiler, U. Giesen, J. Görres, M. Heil, J. Hinnefeld, F. Käppeler, J. J. Kolata *et al.*, Phys. Rev. Lett. **88**, 072501 (2002).
[49] F. C. Barker, Phys. Rev. C **78**, 044611 (2008).
[50] M. La Cognata, V. Z. Goldberg, A. M. Mukhamedzhanov, C. Spitaleri, and R. E. Tribble, Phys. Rev. C **80**, 012801 (2009).
[51] V. Zerkin (2011), http://www-nds.iaea.org/exfor/exfor.htm.
[52] I. V. Mitchell and T. R. Ophel, Nucl. Phys. **58**, 529 (1964).
[53] J. M. Morris, Ph.D. thesis, Australian National University, Canberra, Australia, 1968.
[54] L. Buchmann, R. E. Azuma, C. A. Barnes, J. Humblet, and K. Langanke, Phys. Rev. C **54**, 393 (1996).
[55] R. Kunz, M. Fey, M. Jaeger, A. Mayer, J. W. Hammer, G. Staudt, S. Harissopulos, and T. Paradellis, Astrophys. J. **567**, 643 (2002).
[56] D. Sayre, Ph.D. thesis, Ohio University, 2011.
[57] D. Schürmann, L. Gialanella, R. Kunz, and F. Strieder, Phys. Lett. B **711**, 35 (2012).
[58] P. Martin and T. Ophel, Nucl. Phys. A **202**, 257 (1973).
[59] J. Ramirez and E. Bernstein, Nucl. Phys. A **173**, 207 (1971).
[60] W.-M. Yao, C. Amsler, D. Asner, R. Barnett, J. Beringer, P. Burchat, C. Carone, C. Caso, O. Dahl, G. D'Ambrosio *et al.*, J. Phys. G **33**, 1 (2006).

[61] W. Eadie, D. Drijard, F. James, M. Roos, and B. Sadoulet, *Statistical Methods in Experimental Physics* (North-Holland, Amsterdam, 1971).
[62] W. Press, S. Teukolsky, W. Vetterling, and B. Flannery, *Numerical Recipies: The Art of Scientific Computing*, 3rd ed. (Cambridge University Press, New York, 2007).
[63] H. Costantini, R. J. deBoer, R. E. Azuma, M. Couder, J. Görres, J. W. Hammer, P. J. LeBlanc, H. Y. Lee, S. O'Brien, A. Palumbo *et al.*, Phys. Rev. C **82**, 035802 (2010).
[64] P. Descouvemont, A. Adahchour, C. Angulo, A. Coc, and E. Vangioni-Flam, At. Data Nucl. Data Tables **88**, 203 (2004).
[65] See Supplemental Material at http://link.aps.org/supplemental/10.1103/PhysRevC.87.015802 for the covariance and correlation matrices.
[66] E. Earle and N. Tanner, Nucl. Phys. A **95**, 241 (1967).
[67] H. Lorenz-Wirzba, P. Schmalbrock, H. Trautvetter, M. Wiescher, C. Rolfs, and W. Rodney, Nucl. Phys. A **313**, 346 (1979).
[68] H. W. Becker, M. Bahr, M. Berheide, L. Borucki, M. Buschmann, C. Rolfs, G. Roters, S. Schmidt, W. H. Schulte, G. E. Mitchell *et al.*, Z. Phys. A-Hadron. Nucl. **351**, 453 (1995).
[69] H. Herndl, H. Abele, G. Staudt, B. Bach, K. Grün, H. Scsribany, H. Oberhummer, and G. Raimann, Phys. Rev. C **44**, R952 (1991).
[70] C. R. Brune, W. H. Geist, R. W. Kavanagh, and K. D. Veal, Phys. Rev. Lett. **83**, 4025 (1999).
[71] S. Gorodetzky, J. Adloff, F. Brochard, P. Chevallier, D. Dispier, P. Gorodetzky, R. Modjtahed-Zadeh, and F. Scheibling, Nucl. Phys. A **113**, 221 (1968).